Open access • Journal Article • DOI:10.3847/1538-4357/833/2/254

Inferred Hα Flux as a Star Formation Rate Indicator at z ~ 4-5 : Implications for Dust Properties, Burstiness, and the z = 4-8 Star Formation Rate Functions — Source link

Renske Smit, Renske Smit, Rychard Bouwens, Ivo Labbé ...+3 more authors

Institutions: Leiden University, Durham University, University of Sussex, Yale University

Published on: 20 Dec 2016 - The Astrophysical Journal (Institute of Physics)

Topics: Star formation, Stellar population, Spectral energy distribution and Galaxy

The Astrophysical Journal, 833:254 (20pp), 2016 December 20 doi:10.3847/1538-4357/833/2/254

INFERRED Hα FLUX AS A STAR FORMATION RATE INDICATOR AT $z \sim 4$–5: IMPLICATIONS FOR DUST PROPERTIES, BURSTINESS, AND THE $z = 4$–8 STAR FORMATION RATE FUNCTIONS

Renske Smit[1,2], Rychard J. Bouwens[2], Ivo Labbé[2], Marijn Franx[2], Stephen M. Wilkins[3], and Pascal A. Oesch[4]
[1] Centre for Extragalactic Astronomy, Durham University, South Road, Durham, DH1 3LE, UK
[2] Leiden Observatory, Leiden University, NL-2300 RA Leiden, The Netherlands
[3] Astronomy Centre, Department of Physics and Astronomy, University of Sussex, Brighton BN1 9QH, UK
[4] Yale Center for Astronomy and Astrophysics, Yale University, New Haven, CT 06520, USA
Received 2015 November 20; revised 2016 August 27; accepted 2016 October 17; published 2016 December 20

ABSTRACT

We derive Hα fluxes for a large spectroscopic and photometric-redshift-selected sample of sources over GOODS-North and South in the redshift range $z = 3.8$–5.0 with deep *Hubble Space Telescope* (*HST*), *Spitzer*/IRAC, and ground-based observations. The Hα flux is inferred based on the offset between the IRAC 3.6 μm flux and that predicted from the best-fit spectral energy distribution (SED). We demonstrate that the Hα flux correlates well with dust-corrected UV star formation rate (SFR) and therefore can serve as an independent SFR indicator. However, we also find a systematic offset in the $SFR_{H\alpha}/SFR_{UV+\beta}$ ratios for $z \sim 4$–5 galaxies relative to local relations (assuming the same dust corrections for nebular regions and stellar light). We show that we can resolve the modest tension in the inferred SFRs by assuming bluer intrinsic UV slopes (increasing the dust correction), a rising star formation history, or assuming a low-metallicity stellar population with a hard ionizing spectrum (increasing the $L_{H\alpha}$/SFR ratio). Using Hα as an SFR indicator, we find a normalization of the star formation main sequence in good agreement with recent SED-based determinations and also derive the SFR functions at $z \sim 4$–8. In addition, we assess for the first time the burstiness of star formation in $z \sim 4$ galaxies on <100 Myr timescales by comparing UV and Hα-based sSFRs; their one-to-one relationship argues against significantly bursty star formation histories.

Key words: galaxies: evolution – galaxies: formation – galaxies: high-redshift

1. INTRODUCTION

Over the last decade, dedicated deep field programs with the *Hubble Space Telescope (HST)* have identified more than 10000 candidate galaxies with a redshift beyond $z \gtrsim 4$, based on their photometric colors (e.g., Bouwens et al. 2015). Although a number of these objects have been successfully confirmed out to $z \sim 8.7$ through near-infrared (NIR) spectroscopy (e.g., Finkelstein et al. 2013; Oesch et al. 2015; Zitrin et al. 2015), progress in characterizing the spectral energy distributions (SEDs) of these galaxies and identifying their physical properties has been slow. This is largely due to the fact that spectroscopy and deep, high-resolution photometry in the rest-frame optical wavelengths, shifted to observed mid-infrared (MIR) wavelengths for sources at $z \gtrsim 4$, will not be available until the launch of the *James Webb Space Telescope (JWST)*.

Despite these challenges, a number of noteworthy results have emerged on the observational properties of the $z \gtrsim 4$ galaxy population. First of all, the typical rest-frame UV colors of galaxies from $z \sim 4$ to $z \sim 8$ have been meticulously characterized through their *HST* photometry (Bouwens et al. 2009, 2012, 2014; Wilkins et al. 2011; Dunlop et al. 2012, 2013; Finkelstein et al. 2012). Furthermore, photometric studies using the *Spitzer Space Telescope* have obtained the first constraints on the shape of the rest-frame optical SED of $z \gtrsim 4$ galaxies (Eyles et al. 2005; Verma et al. 2007; Wiklind et al. 2008; Stark et al. 2009; Yabe et al. 2009; González et al. 2010, 2012; Labbé et al. 2010a, 2010b). In particular, observational evidence has emerged for the presence of strong optical nebular emission lines, such as Hα and [O III], in the typical $z \gtrsim 4$ sources (Schaerer & de Barros 2009; Shim et al. 2011; Labbé et al. 2013; Stark et al. 2013; de Barros et al. 2014; González et al. 2014; Smit et al. 2014; Mármol-Queraltó et al. 2016; Rasappu et al. 2015; Roberts-Borsani et al. 2016; Smit et al. 2015).

While the rest-frame equivalent widths (EWs) of Hα in typical star-forming galaxies at $z \sim 0$–2 are in the range 10–200 Å (Fumagalli et al. 2012), a large fraction of sources between $z \sim 4$–8 have inferred Hα and [O III] EWs in the ranges 250–600 Å and 600–1000 Å, respectively (Schaerer & de Barros 2009; Shim et al. 2011; Labbé et al. 2013; Stark et al. 2013; de Barros et al. 2014; González et al. 2014; Smit et al. 2014; Mármol-Queraltó et al. 2016; Rasappu et al. 2015; Smit et al. 2015). These measured EWs are higher than predicted by models of galaxy formation (e.g., Wilkins et al. 2013b) and the origin of these ubiquitous high EW lines is still unclear and proves to be an ongoing challenge for our current understanding of the physical properties of high-redshift galaxies.

While the interpretation of the [O III] line strength is complicated by the dependence on, for example, the gas density in the H II regions (e.g., Kewley et al. 2013; Shirazi et al. 2014), the Hα line strength is known to be stable against variations in density or temperature and therefore should be a stable tracer of the star formation (Kennicutt 1998). Shim et al. (2011) consider the derived Hα fluxes from a spectroscopic sample of sources in the range $z = 3.8$–5.0, where Hα falls into the 3.6 μm *Spitzer*/IRAC filter, and find that the inferred Hα flux in their spectroscopic sample is particularly elevated relative to the inferred star-formation rate (SFR) from the UV continuum. Shim et al. (2011) argue that one probable explanation for the high ratio of Hα flux to UV flux they observe could be due to a preference for young ages among their selected sources, as essentially all sources with spectroscopic redshifts that they consider show Lyα emission. While this speculation by Shim et al. (2011) is reasonable, the actual

impact of considering only those sources showing Lyα emission is unclear; it requires testing based on a much larger and unbiased sample of $z \sim 4$ galaxies and one also benefitting from even deeper photometric observations.

In this paper we revisit the use of Hα as an SFR indicator in the redshift range $z = 3.8$–5.0, considering both expanded spectroscopic and photometric-redshift selections. In doing so, we leverage even deeper *Spitzer*/IRAC coverage from the S-CANDELS survey (Ashby et al. 2015) and deep *K*-band data (Kajisawa et al. 2006; Hathi et al. 2012; Fontana et al. 2014). This approach allows us to make a state-of-the-art assessment on the origin of high-EW Hα emission in typical high-redshift sources.

We search for correlations of the Hα EW with a large number of observational and physical properties, and we look for possible biases in the results of spectroscopic samples relative to photometric-redshift-selected samples and vice versa. We use the Hα fluxes to derive specific star formation rates from galaxies and compare these rates to the sSFRs derived from the UV-continuum fluxes in an effort to constrain the burstiness of the star formation history. Finally, we discuss the implications of our results for the main sequence of star-forming galaxies and the $z \sim 4$–8 SFR functions.

This paper is organized as follows. In Section 2 we describe the observations we use and how we define our spectroscopic and photometric-redshift-selected samples, while we derive the observational and physical properties of our samples in Section 3. In Section 4 we derive Hα-based SFRs, which we compare with UV-based SFRs, and we discuss the potential origin of the discrepancy we find between the different probes. In Section 6.1 we establish the main sequence of star-forming galaxies from our Hα measurements, while in Section 6.2 we translate our findings into SFR functions. Finally, we summarize our results in Section 7.

Throughout this paper we adopt a Salpeter initial mass function (IMF) with limits 0.1–100 $M_{\odot}$ (Salpeter 1955). For ease of comparison with previous studies we take $H_0 = 70$ km s^{-1} Mpc^{-1}, $\Omega_m = 0.3$, and $\Omega_\Lambda = 0.7$. Magnitudes are quoted in the AB system (Oke & Gunn 1983).

2. DATA AND SAMPLES

2.1. Spectroscopic Redshift Sample

For our main sample of $z \sim 4$ galaxies we take advantage of the spectroscopic redshift information collected over the GOODS-N and GOODS-S found in the public samples of Shim et al. (2011), Stark et al. (2013), Balestra et al. (2010), Vanzella et al. (2005, 2006, 2008), and Vanzella et al. (2009). These authors have collected galaxy samples from spectroscopic follow-up of *B*- and *V*-drop selected galaxy candidates, typically using i_{775} or I_C as the detection band. Redshifts for these galaxies are mainly derived from the position of the Lyα emission line, although redshifts for a few bright galaxy candidates are derived from their UV absorption lines or continuum breaks.

We select sources with secure spectroscopic redshifts between $z = 3.8$ and $z = 5.0$, the redshift range where the Hα line contributes to the flux in the 3.6 μm band, while the 4.5 μm band is free of contamination from strong nebular lines (see Shim et al. 2011; Stark et al. 2013). Within this redshift range the *K* band is largely free of strong emission lines such as [O III], Hα, and Hβ, though the [O II]λ3727 Å emission line could result in a boost to the *K*-band flux (~0.1–0.2 mag) for galaxies between $z = 4.35$ and $z = 5.0$ (affecting 43% of our sample).

We obtain photometry for the sources in our sample by matching the spectroscopic $z = 3.8$–5.0 sample with the public 3D-*HST*/CANDELS catalogs presented by Skelton et al. (2014). We utilize their measured photometry in all *HST* bands (B_{435}, V_{606}, i_{775}, I_{814}, z_{850}, J_{125}, JH_{140} and H_{160}). The median 5σ limiting magnitude in the bands, measured in a 0.″7 diameter aperture, ranges from 25.6 to 27.4. In short, Skelton et al. (2014) obtain their photometry by running Source Extractor (Bertin & Arnouts 1996) in dual image mode on all bands and by matching their point-spread function (PSF) to the H_{160}-band PSF. A combination of the J_{125}, JH_{140} and H_{160} images is used as the detection image (weighted by the square root of the inverse variance) and total fluxes are measured in Kron apertures.

Furthermore, we include the photometry in the *Spitzer*/IRAC bands at 5.8 and 8.0 μm from the Skelton et al. (2014) photometric catalogs, who make use of the GOODS Spitzer 3rd data release. We obtain the deepest possible photometry for the 3.6 μm and 4.5 μm bands by leveraging the imaging from the Spitzer Extended Deep Survey (SEDS: Ashby et al. 2013) and the Spitzer Very Deep Survey Exploration Science Project (S-CANDELS: Ashby et al. 2015), which covers the GOODS-N and GOODS-S fields with up to 50 hr exposure times (26.8 mag at 5σ in a 2.″0 diameter aperture in the 3.6 μm band). Following the procedure used for the public 3D-*HST*/CANDELS catalog (described in Skelton et al. (2014), we obtain photometry using the Multi-resolution Object PHotometry oN Galaxy Observations (MOPHONGO) code described in Labbé et al. (2006, 2010a, 2010b, 2015), which provides an automated cleaning procedure for deblending the sources of interest and their neighboring sources. In short, MOPHONGO creates model fluxes for all sources in an ~11″ radius by PSF-matching all detected galaxies in the H_{160} band to the IRAC image PSF and simultaneously fitting the normalizations of the modeled galaxies to match the observed IRAC image. Cleaned images are created by subtracting the model fluxes of all neighboring sources from the observed image. We measure the flux in the 3.6 and 4.5 μm bands from the cleaned images in 2.″0 diameter apertures and we apply a ~2.2–2.4× aperture correction based on the ratio of the flux enclosed in the photometric aperture in the *HST* image (before convolution) to the IRAC model (after convolution) of the source of interest.

In order to obtain good constraints on the rest-frame optical stellar light, both shortward and longward of the Hα emission line, we require good signal-to-noise *K*-band photometry. For the GOODS-N field we therefore combine CFHT/WIRCam K_s-band imaging (Hathi et al. 2012) and *Subaru*/MOIRCS K_s-band imaging (Kajisawa et al. 2006). For the GOODS-S field we combine deep FOURSTAR K_s-band imaging from the Z-FOURGE survey (Spitler et al. 2012), VLT/ISAAC K_s-band imaging from the FIREWORKS survey (Retzlaff et al. 2010), and VLT/HAWK-I K_s-band imaging from the HUGS survey (Fontana et al. 2014). We use MOPHONGO to perform an identical deblending procedure to that described in the previous paragraph and we perform photometry on the cleaned images in 1.″0 diameter apertures. The median 5σ limiting depths are 24.8 and 25.2 mag (in a 1.″0 diameter aperture) in GOODS-N

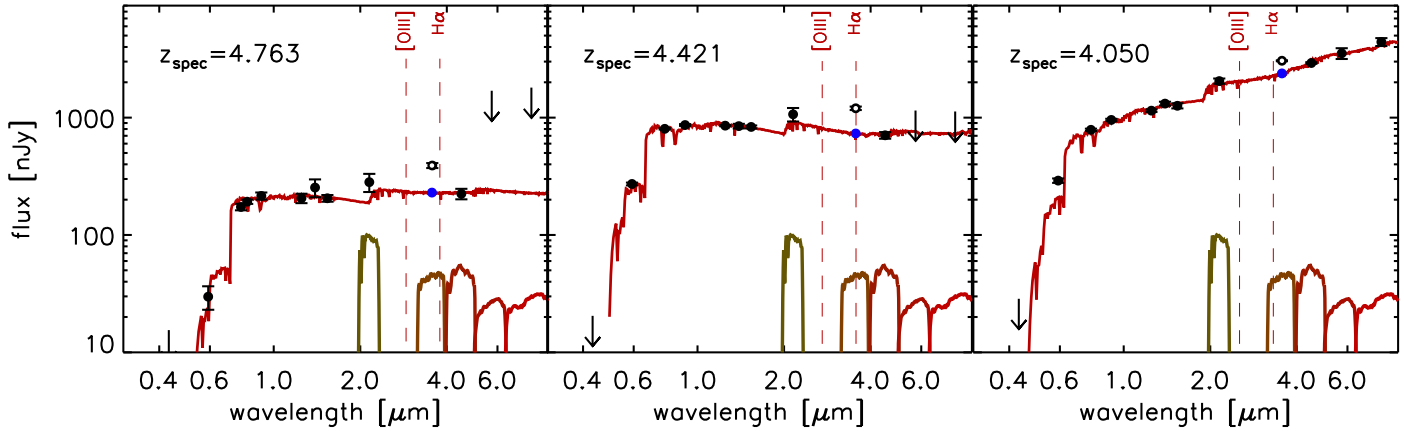

Figure 1. Three examples of stellar population fits to the broadband observations of galaxies from our sample. Flux densities and upper limits (2σ) of the *HST*, ground-based, and *Spitzer*/IRAC photometry are indicated with black points and arrows, while the best-fit stellar population (Section 3.1) is drawn in red. Filter transmission curves of the rest-frame optical bands are drawn to show the coverage of the SED. The IRAC 3.6 μm band flux is contaminated by Hα, [N II], and [S II] and is not included in the SED fitting (open points). The 4.5 μm band is largely free of line contamination and therefore provides the most important constraint on the stellar continuum at rest-frame visible wavelengths. The offset between the predicted 3.6 μm continuum flux from the SED (indicated by the blue points) and the observed 3.6 μm flux provides a good estimate of the total Hα+[N II]+[S II] line flux.

and GOODS-S, respectively; 44% of our spectroscopic sample is detected at $>5\sigma$ in the K_s band.

Our resulting catalog of $z_{\rm spec} = 3.8$–5.0 galaxies consists of 37 sources in GOODS-N and 53 sources in GOODS-S, with high-quality constraints on the SEDs of the galaxies. The SEDs of three typical galaxies are presented in Figure 1.

2.2. Photometric-Redshift Sample

We complement our spectroscopic redshift sample with a high-confidence photometric sample to add valuable statistics. Using a photometric-redshift-selected sample is also valuable to evaluate potential biases in the spectroscopic sample that may arise owing to these samples being predominantly composed of galaxies that show Lyα in emission. For this photometric sample we utilize the public photometric-redshift catalog over the GOODS-S field from the 3D-*HST*/CANDELS data release (Skelton et al. 2014), generated using the EAZY software (Brammer et al. 2008). We require selected sources to have a photometric redshift within the redshift range $z = 3.8$–5.0 with at least 99% probability. Of the sample of sources that satisfy the 99% probability criterion, 84% have a best-fit photometric-redshift template with a reduced χ^2 value of less then 3 (95% has a $\chi^2_{\rm red} < 5$). Of the sources in the spectroscopic sample, 71% satisfy this criterion, and the remaining 29% have a spectroscopic redshift at the edges of the $z = 3.8$–5.0 redshift range used for selection.

We assemble the photometry for our photometric sample in an identical way to the spectroscopic sample as described in Section 2.1. We apply a luminosity cut for our main sample below $H_{160} < 26.5$ in order to ensure high-S/N IRAC photometry for our entire sample. This results in a photometric catalog containing 320 sources. Furthermore, we include an i_{775} limited subsample that we use to investigate the bias of our spectroscopic sample in the derived galaxy properties with respect to our photometrically selected sources. For this subsample we use $i_{775} < 25.4$ (80 sources) in order to match as closely as possible the median i-band luminosity of our photometric to the median of the spectroscopic sample ($i_{775} = 25.1$). In the main photometric-redshift-selected sample, 64 sources are included that are also part of the spectroscopic sample. For the remainder of the paper, we quote numbers for the separate selections with these spectroscopically confirmed sources included. However, when quoting measured quantities for the combined sample, we only count a given source once (even if it is found in both samples).

We compare the observational properties of our i_{775}-band limited photometric-redshift-selected subsample with the spectroscopic sample in Figure 2. The UV-continuum colors are parametrized using the UV-continuum slope β, with $f_\lambda \propto \lambda^\beta$. The β-slope is approximated by a log-linear fit to the z_{850}, J_{125}, JH_{140} and H_{160} fluxes (Bouwens et al. 2012; Castellano et al. 2012). The differences in the median UV-continuum color and the $H_{160} - [4.5]$ color between our i_{775}-band limited photometric subsample and our spectroscopic sample are consistent within the bootstrapped uncertainties. We therefore conclude that the spectroscopic sample targeting mainly Lyα emitters has no obvious bias with respect to a photometric-redshift-selected sample, given similar i_{775}-band luminosities (see also Schenker et al. 2013).

In Section 3.1 we remove those sources with bad SED fitting, which results in a final sample size of 80 sources in the spectroscopic and 302 sources in the photometric catalog. We tabulate the properties of our final spectroscopic and photometric-redshift-selected samples in Table 1.

3. DERIVED PROPERTIES OF $z = 3.8$–5.0 GALAXIES

3.1. SED Fitting

We determine stellar masses and other stellar population parameters by fitting stellar population synthesis templates to the observed photometry using FAST (Kriek et al. 2009). We do not include emission lines in our galaxy templates; instead we consider only stellar continuum in our models, while we exclude from our fitting procedure the 3.6 μm band, where Hα, [N II], and [S II] boosts the observed flux. We consider constant star formation histories with ages between 10 Myr and the age of the universe at $z = 3.8$. Furthermore, we assume a Calzetti et al. (2000) dust law with A_V in the range 0–2. Finally, we

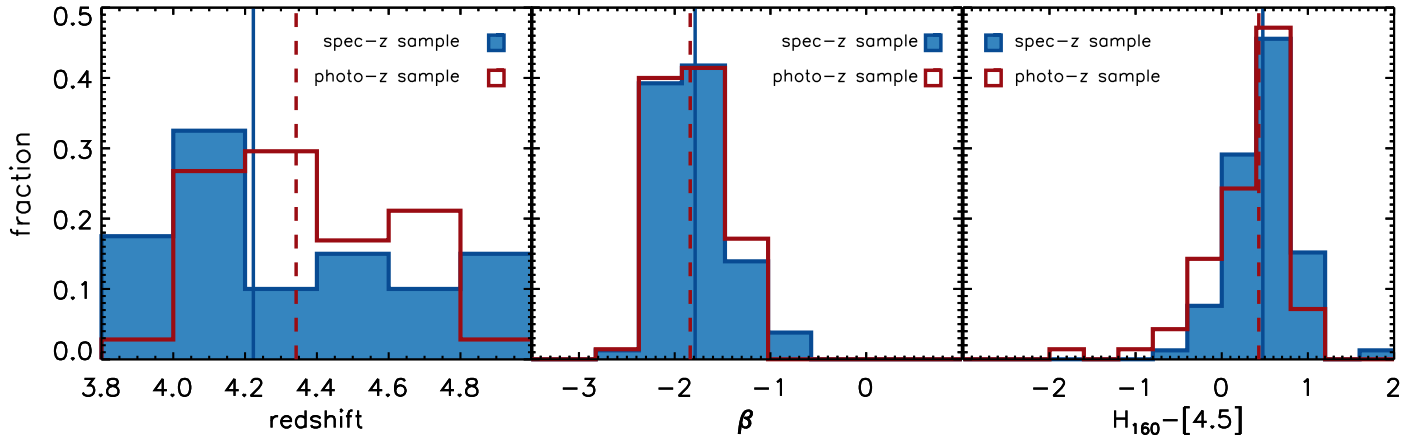

Figure 2. Comparison of the observational properties of the i_{775}-band limited photometric-redshift-selected subsample (filled blue histograms) and the spectroscopic-redshift-selected (red histograms) sample. The solid blue lines and dashed red lines indicate the median values for the spectroscopic and photometric-redshift-selected samples, respectively. The median i_{775}-band magnitudes of the two samples are identical by construction thanks to our $i_{775} \lesssim 25.4$ luminosity cut on the photometric-redshift-selected sample (see Section 2.2). Left panel: the redshift distribution of the two samples. We find a median $\langle z_{\rm spec} \rangle \sim 4.25$ and a median $\langle z_{\rm phot} \rangle \sim 4.38$. Middle panel: the UV-continuum slope, β, defined as $f_\lambda \propto \lambda^\beta$. The median UV-continuum slope of the spectroscopic sample is slightly bluer than the median slope for the photometric-redshift-selected sample. Right panel: the $H_{160} - [4.5]$ color, where the H_{160} band probes the rest-frame UV-continuum and the 4.5 μm band gives a measure of the rest-frame optical continuum flux. The medians of the two samples are within the errors. Overall, the colors of the SEDs of the spectroscopic sample show very little bias when compared to the photometric-redshift-selected sample with the same median i_{775}-band luminosity even though the majority of our spectroscopic redshifts are obtained from Lyα in emission.

allow the metallicities to range between 0.2 and 1.0 $Z_\odot$ in the fits.

We fix the redshifts in the SED fitting either to the spectroscopic redshift of the galaxies or to the photometric-redshift value used to select galaxies in the photometric-redshift sample (Section 2.2). Note that when we let the redshift of the galaxies in the photometric sample float, the estimated median EW$_0$(Hα+[N II]+[S II]) changes by only +0.01 dex. For a small number of galaxies we find a bad fit to the photometry and we therefore remove 9 sources from the spectroscopic sample and 18 sources from the photometric-redshift sample when the reduced χ^2 is greater than 4.

Our estimated median stellar mass is $4.4 \cdot 10^9\,M_\odot$ for our main spectroscopic sample and $1.6 \cdot 10^9\,M_\odot$ for our photometric sample, reflecting the fact that our main photometric sample extends to lower luminosities.

3.2. Hα+[N II]+[S II] Equivalent Widths and Line Strengths

We infer the total emission line flux in our sources from the 3.6 μm band by subtracting the predicted continuum fluxes of the best-fit stellar templates (see Figure 1) from the observed 3.6 μm fluxes. A correction is made for the width of the 3.6 μm filter using the spectral response curve of this filter[5] (see also Shim et al. 2011; Stark et al. 2013). We estimate the uncertainty on the predicted continuum flux to be equal to the uncertainty on the 4.5 μm-band flux, and therefore the uncertainty on the flux offset in the 3.6 μm band is equal to the uncertainty in the [3.6]–[4.5] color. If the uncertainty on the line flux is larger than the offset between the observed 3.6 μm flux and the predicted continuum, we place an upper limit on the line flux.

Since the total emission line flux is dominated by the contribution from Hα, [N II], and [S II] (e.g., Anders & Fritze-v. Alvensleben 2003) we directly obtain rest-frame equivalent widths (EW$_0$) for these lines based on the inferred total emission line flux and the predicted continuum of the best-fit stellar template after correcting the observed EW by a factor $(1 + z)$. Here we use the FAST redshift estimates for the photometric sample. We find EW$_0$(Hα+[N II]+[S II]) ~399–429 Å in the median source of our samples. We did not correct the continuum emission or line emission for dust attenuation.

Our estimate of the equivalent width is in good agreement with Stark et al. (2013), who measure $\langle \log_{10}(\mathrm{EW}_{3.6\,\mu\mathrm{m}}) \rangle \sim 2.57$–$2.73$ in the rest-frame. The present result is ~20% higher than recent results by Mármol-Queraltó et al. (2016), but this may be due to the fact that the median stellar mass for our sample is ~0.9 dex lower than the sample considered by Mármol-Queraltó et al. (2016) and a possible correlation of the Hα EW with stellar mass ($\mathrm{EW}_{\mathrm{H}\alpha} \propto M_*^{-0.25}$: Fumagalli et al. 2012; Sobral et al. 2014).[6] Furthermore, our estimate is lower than the $z \sim 5$ estimate of the equivalent width by Rasappu et al. (2015), who derive ~665 Å from the median [3.6]–[4.5] color. The difference between the $z \sim 4.3$ to $z \sim 5.2$ equivalent width estimates is consistent with an evolution of $EW_0 \propto (1 + z)^{1.8}$ within $<2\sigma$ (Fumagalli et al. 2012; Sobral et al. 2014). Shim et al. (2011) derive a much higher EW$_0$(Hα+[N II]+[S II]) ~ 600 Å over the same redshift range, using a similar method of deriving Hα fluxes. We have 52 sources in common with the Shim et al. (2011) sample, but using our method we find a median EW$_0$(Hα +[N II]+[S II]) = 416 Å for these sources. We find that our lower EW measurements for the same sources are possibly due to a systematically lower 3.6 μm flux (Δ([3.6]–[4.5]) = 0.21 ± 0.08 mag) than used by Shim et al. (2011). Mármol-Queraltó et al. (2016) also find a

[5] http://irsa.ipac.caltech.edu/data/SPITZER/docs/irac/calibrationfiles/spectralresponse/

[6] However, the apparent correlation of the Hα EW with stellar mass could be significantly impacted by source selection and the fact that the lowest sSFR, lowest mass sources simply could not be selected and included in current samples. See Figure 11.

Table 1
Median Properties of the Spectroscopic and Photometric-redshift-selected Samples

	N	z	$M_{\rm UV}$	M_* ($M_\odot$)	β	EW$_0$[a] (Hα) (Å)	EW$_0$[a] (Hα+[N II]+[S II]) (Å)	sSFR$_{\rm UV}$[a,b] (Gyr^{-1})	sSFR$_{\rm H\alpha}$[a,b] (Gyr^{-1})
spec-z	80	4.3	−21.1	$4.0 \cdot 10^9$	−1.79	361 ± 19	429 ± 23	13.3 ± 0.6	16.7 ± 3.4
photo-z (all)	302	4.4	−20.3	$1.5 \cdot 10^9$	−1.79	335 ± 22	399 ± 27	15.1 ± 1.1	17.6 ± 2.0
photo-z ($i_{775} < 25.4$)	71	4.4	−21.1	$3.2 \cdot 10^9$	−1.84	269 ± 80	320 ± 96	15.1 ± 1.8	14.5 ± 4.6
photo-z ($\log_{10}M_* > 9.5$)	88	4.4	−20.7	$5.5 \cdot 10^9$	−1.62	220 ± 38	262 ± 46	5.7 ± 1.0	5.8 ± 1.1

Notes.
[a] Measured median values and uncertainties obtained from bootstrapping.
[b] Corrected for dust using the UV slope β and the Meurer et al. (1999) calibration; Hα is corrected for dust assuming $A_{V,\rm stars} = A_{V,\rm gas}$ and using the Calzetti et al. (2000) dust curve.

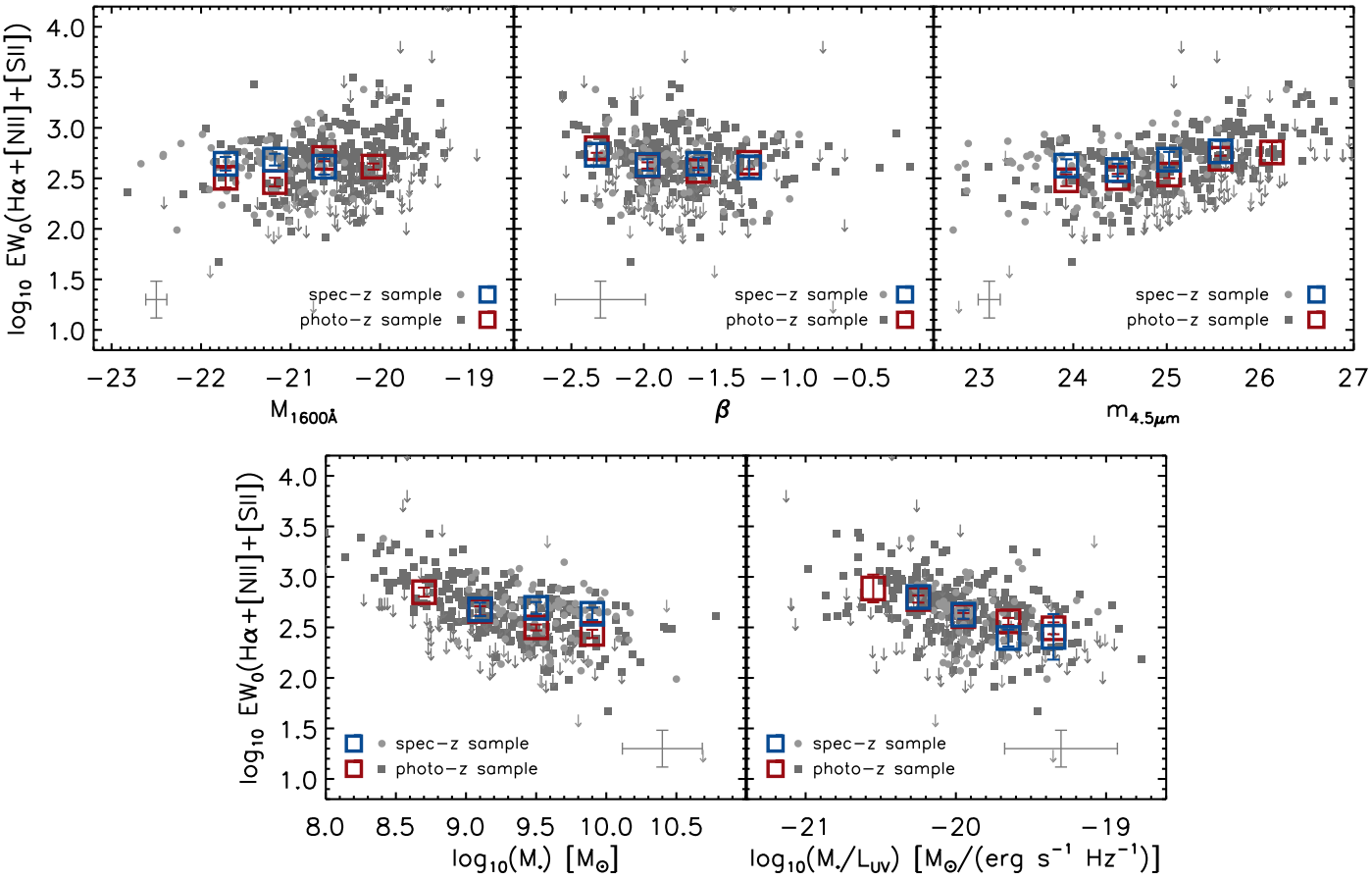

Figure 3. The rest-frame Hα+[N II]+[S II] EWs of our spectroscopic (light gray points) and our main photometric-redshift-selected sample (dark gray squares) measured from the offsets in the observed 3.6 μm flux with respect to the predicted stellar continuum (see Section 3.2). Error bars for individual points are not shown to improve the clarity of the figures; instead, representative error bars are shown at the bottom of each panel. The left, middle, and right panels show the dependence of EW$_0$(Hα+[N II]+[S II]) as a function of the observed UV luminosity (measured at 1600 Å from the best-fit stellar template), the UV-continuum slope β, and the observed [4.5] magnitude, respectively. The blue and red squares indicate the median EWs (error bars represent the uncertainty in the median). We explore the dependence of the median emission line EW on the UV luminosity, UV-continuum slope β, observed [4.5] magnitude, stellar mass, and mass-to-light ratio. The emission line EW is clearly correlated with $M_*/L_{\rm UV}$ in both the spectroscopic and photometric samples, indicating that the EWs might be mainly driven by the star formation activity in the galaxy.

0.2 mag discrepancy with the 3.6 μm photometry used by Shim et al. (2011).

We show the distribution of the resulting EWs as a function of the UV-luminosity (measured at 1600 Å from the best-fit stellar template), the UV-continuum slope β, and the observed 4.5 μm-band magnitude in the top panels of Figure 3. We use a linear fit to the median bins in Figure 3, where we bootstrap every bin 1000 times and re-fit a linear relation to obtain realistic errors on the linear slope. We list the slopes and bootstrapped uncertainties in Table 2. With this method, we find that EW$_0$(Hα+[N II]+[S II]) in our spectroscopic sample is consistent (at $\lesssim 2\sigma$) with no correlation for all distributions in Figure 3. In the photometric-redshift-selected sample, the typical derived EW$_0$(Hα+[N II]+[S II]) seems to be weakly dependent on β and on the observed 4.5 μm-band magnitude (at the $\sim 2\sigma$–3σ level).

To gain further insight into the possible physical origin for these high EW lines, we use the public catalogs with structural parameters presented by van der Wel et al. (2012, 2014) to identify potential correlations with our Hα measurements.

Table 2
Dependence of EW_0(Hα+[N II]+[S II]) on Observational Properties[a]

	spec-z	photo-z
$d\ \log_{10}EW_{0,H\alpha+[N\ II]+[S\ II]}/d\ M_{UV}$	$0.08^{+0.13}_{-0.14}$	$0.08^{+0.04}_{-0.08}$
$d\ \log_{10}EW_{0,H\alpha+[N\ II]+[S\ II]}/d\ \beta$	$0.08^{+0.20}_{-0.20}$	$-0.17^{+0.06}_{-0.07}$
$d\ \log_{10}EW_{0,H\alpha+[N\ II]+[S\ II]}/d\ m_{4.5\mu m}$	$0.01^{+0.09}_{-0.08}$	$0.14^{+0.05}_{-0.04}$
$d\ \log_{10}EW_{0,H\alpha+[N\ II]+[S\ II]}/d\ \log_{10}M_*$	$0.12^{+0.17}_{-0.23}$	$-0.35^{+0.08}_{-0.07}$
$d\ \log_{10}EW_{0,H\alpha+[N\ II]+[S\ II]}/d\ \log_{10}(M_*/L_{UV})$	$-0.09^{+0.25}_{-0.24}$	$-0.36^{+0.06}_{-0.07}$

Note.
[a] Measured linear slopes from the median binned data. Uncertainties are obtained from bootstrapping the binned data and re-fitting a linear slope to each bootstrapped set of medians.

However, we find no dependence of EW_0(Hα+[N II]+[S II]) on the half-light radius or the Sérsic index.

Furthermore, we study the dependence of Hα EW on the parameters from our stellar population modeling (Section 3.1) in the bottom panels of Figure 3. For our photometric-redshift-selected sample we find a dependence of EW_0(Hα+[N II]+[S II]) on stellar mass and M_*/L_{UV} (at $\gtrsim 5\sigma$), which is expected if the Hα is predominantly determined by the star formation activity in the galaxy.

Therefore we explore the use of our inferred Hα measurements as an SFR indicator in the next section. To do this, we derive an estimate of the Hα line flux by adopting a fixed ratio between Hα, [N II], and [S II] as tabulated in Anders & Fritze-v. Alvensleben (2003) for subsolar ($0.2\ Z_\odot$) metallicity, i.e., $L_{H\alpha} = 0.84 \times L_{3.6\mu m}$, where $L_{3.6\mu m}$ is the total luminosity derived from the offset in the 3.6 μm band with respect to the estimated continuum from the SED. This is consistent with the findings of Sanders et al. (2015), who observe a ratio of N II/Hα of 0.05–0.09 in $z \sim 2.3$ galaxies with stellar masses in the range $\log(M_*/M_\odot) = 9.15$–9.94. The resulting Hα EW is 361 Å for our spectroscopic and 335 Å for our photometric-redshift-selected sample.

3.3. Composite SEDs

Our spectroscopic sample is particularly well suited to constructing composite SEDs of star-forming galaxies over the redshift range $z = 3.8$–5.0. Figure 4 shows three composite SEDs; the galaxies are divided into different samples based on their estimated EW_0(Hα+[N II]+[S II]). The flux measurements are normalized on the z_{850}, H_{160}, and 4.5 μm bands. By construction the offset in the flux measurements around the Hα line increases from bottom to top. We find the highest EW_0(Hα+[N II]+[S II]) to have a slightly bluer and lower mass SED, consistent with the relations in Table 2 for the photometric sample.

4. INFERRED Hα AS A STAR FORMATION RATE INDICATOR

Our determination of the Hα line flux in Section 3.2 provides us with the unique opportunity to explore the use of inferred Hα fluxes as an independent star formation rate indicator in high-redshift galaxies. Shim et al. (2011) pioneered the use of inferred Hα to measure SFRs of $z \sim 4$ galaxies. However, the exceptionally deep S/N Spitzer/IRAC data from the S-CANDELS data set (Ashby et al. 2015) covering our large spectroscopic and photometric-redshift-selected samples allows us to systematically assess the SFRs over the general $z \sim 4$ galaxy population.

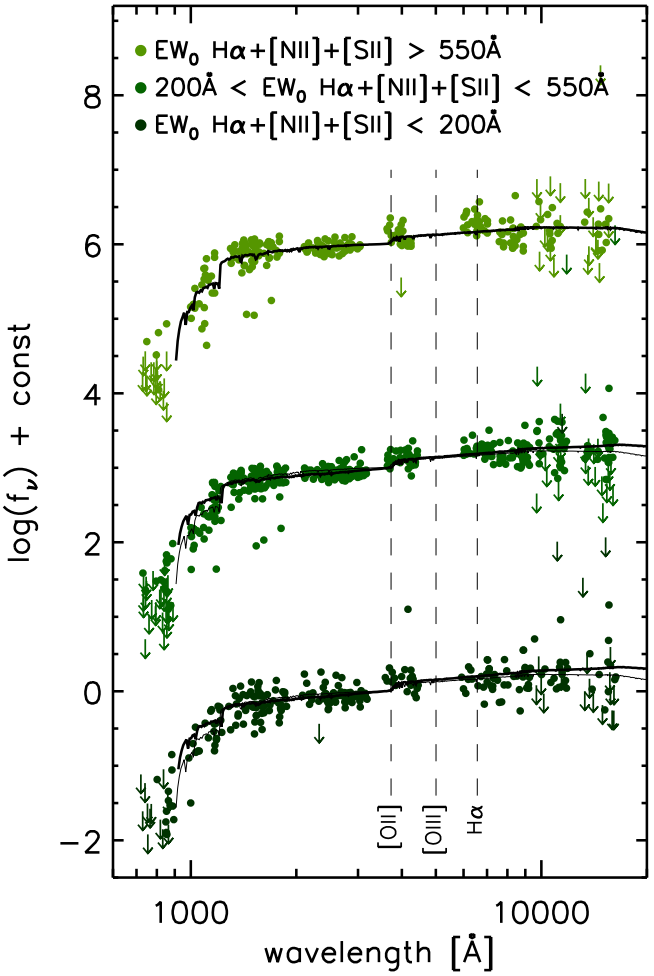

Figure 4. Composite spectral energy distributions of the sources in the spectroscopic sample shown as a function of the rest-frame wavelengths (green points). The sources presented in the top, middle, and bottom SEDs have estimated EW_0(Hα+[N II]+[S II]) that are greater than 550 Å, between 200 Å and 550 Å, and less than 200 Å, respectively. The SEDs are offset in the *y*-axis for clarity. All points are normalized by the log mean of the z_{850}, H_{160}, and 4.5 μm fluxes. The dashed black lines indicate the position of the [O II], [O III], and Hα nebular lines. The thick black curves indicate a stellar continuum fit to the composite SEDs. The continuum SED for the highest EW sources is indicated with thin black curves next to the middle and bottom SEDs for reference. From the composite SEDs, high EW sources are slightly bluer and have lower mass, consistent with the results in Section 3.2.

4.1. Star Formation Rate Indicators

In this section we define two independent SFR indicators based on the Hα and UV properties of our samples, using calibrations of local star-forming galaxies. The comparison of these two probes allows us to investigate the different timescales of star formation since Hα is sensitive to the star formation history (SFH) over a ∼10 Myr timescale, while UV light provides a time-averaged SFR over a ∼100 Myr time window (e.g., Kennicutt 1998).

To obtain UV-based SFRs we convert the UV-luminosity measured at 1600 Å from the best-fit stellar template into an

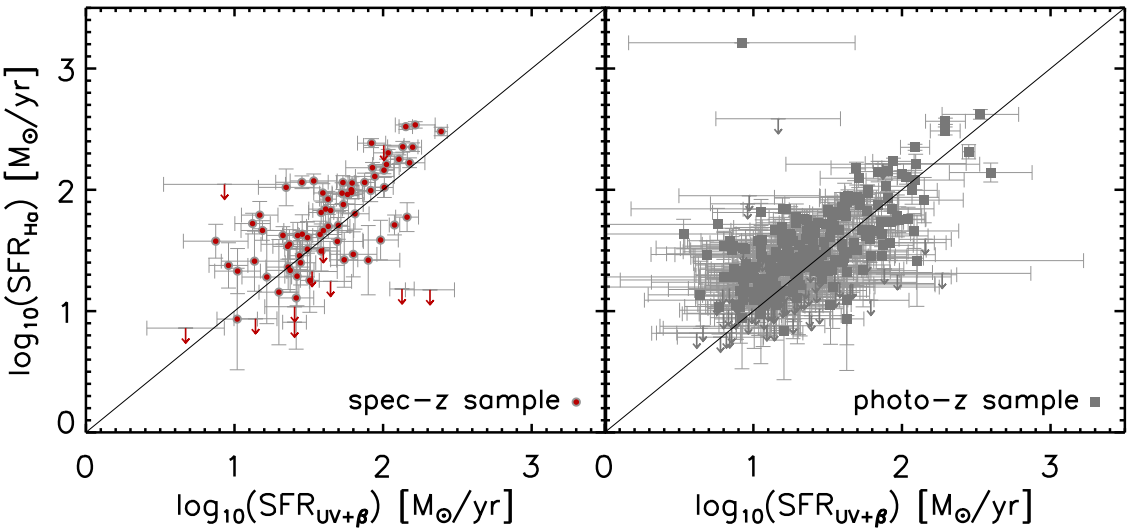

Figure 5. Star formation rates from the inferred Hα luminosities vs. those from the UV-luminosity corrected for dust using the UV slope β and the Meurer et al. (1999) calibration (red points; red arrows indicate the 1σ upper limits); Hα is corrected for dust assuming $A_{V,\mathrm{stars}} = A_{V,\mathrm{gas}}$ and using the Calzetti et al. (2000) dust curve. The left panel shows our spectroscopic sample, while the right panel shows our photometric sample. The median SFRs are offset from the one-to-one relation (black line) by ∼0.15 dex.

SFR using the Kennicutt (1998) relation

$$\mathrm{SFR}(M_\odot\ \mathrm{yr}^{-1}) = 1.4 \times 10^{-28}\, L_{\mathrm{UV}}(\mathrm{erg\ s}^{-1}\,\mathrm{Hz}^{-1}). \quad (1)$$

We estimate the dust attenuation in the UV from the calibration by Meurer et al. (1999) using local starbursting systems

$$A_{1600} = 4.43 + 1.99 \cdot \beta, \quad (2)$$

where we estimate the UV-continuum slope β using a log-linear fit to the z_{850}, J_{125}, JH_{140}, and H_{160} fluxes. Our estimated median dust corrected UV-based SFR ($\mathrm{SFR}_{\mathrm{UV}+\beta}$) is equal to $\sim$43 $M_\odot$ yr^{-1} for our spectroscopic-redshift-selected sample and $\sim$20 $M_\odot$ yr^{-1} for our photometric-redshift-selected sample. We explicitly do not estimate our UV-based SFRs from the SED fitting procedure owing to the degeneracy between age and dust that is particularly challenging to solve. However, we discuss the impact of different calibrations of the dust law on the UV-based SFRs in Section 5.1.

To obtain SFRs from the Hα line luminosity measurements derived in Section 3.2 we use the Kennicutt (1998) relation

$$\mathrm{SFR}(M_\odot\ \mathrm{yr}^{-1}) = 7.9 \times 10^{-42}\, L_{\mathrm{H}\alpha}(\mathrm{erg\ s}^{-1}). \quad (3)$$

We estimate the dust attenuation from the Calzetti et al. (2000) dust law and the UV dust attenuation derived using Equation (2). Here we assume $A_{V,\mathrm{stars}} = A_{V,\mathrm{gas}}$, which is expected to be a reasonable assumption for blue galaxies where both the stars and emission lines are in the birth clouds; it is also found to be a reasonable approximation in $z \sim 2$ galaxies (e.g., Erb et al. 2006; Reddy et al. 2010; Shivaei et al. 2015). Local observations of star-bursting systems indicate $A_{V,\mathrm{stars}} = 0.44 \cdot A_{V,\mathrm{gas}}$ (e.g., Calzetti 1997). However, as we show below, our Hα SFRs are already relatively high compared to our UV-continuum-based SFRs, a discrepancy that would significantly increase if we made the assumption that $A_{V,\mathrm{stars}} = 0.44 \cdot A_{V,\mathrm{gas}}$. Our estimated median SFR from Hα ($\mathrm{SFR}_{\mathrm{H}\alpha}$) after dust correction is equal to $\sim$50 $M_\odot$ yr^{-1} for our spectroscopic sample and $\sim$23 $M_\odot$ yr^{-1} for our photometric sample.

We compare $\mathrm{SFR}_{\mathrm{UV}+\beta}$ and $\mathrm{SFR}_{\mathrm{H}\alpha}$ indicators in Figure 5 and we find that the two indicators are strongly correlated in both the spectroscopic and photometric samples. This strong correlation suggests that our method of inferring Hα line measurements from the broadband IRAC photometry can be used as a tracer of star formation. However, we also find a systematic offset of $0.16^{+0.03}_{-0.04}$ dex for our spectroscopic sample and $0.10^{+0.03}_{-0.01}$ dex for our photometric-redshift-selected sample (see also Figure 6) from the one-to-one relation (uncertainties obtained from bootstrapping). Had we assumed a differential dust attenuation between nebular light and starlight, i.e., $A_{V,\mathrm{stars}} = 0.44 \cdot A_{V,\mathrm{gas}}$, these offsets would have increased to ∼0.3 dex.

We have investigated potential systematics in our method of obtaining Hα flux measurements that could explain the offset between $\mathrm{SFR}_{\mathrm{UV}+\beta}$ and $\mathrm{SFR}_{\mathrm{H}\alpha}$. In Appendix A we present two tests performed at $z < 3.8$ to check for systematics in the photometry and the SED fitting used in this paper. First, we compared spectroscopically measured emission lines with line fluxes inferred from the broadband photometry with the same method we use for our $z = 3.8$–5.0 samples. We use Hα+[N II] fluxes from galaxies in the 3D-*HST* grism survey at $z = 1.3$–1.5 (Momcheva et al. 2016). We find no significant offset in the median sources between spectroscopically measured line fluxes and the flux measurements inferred from the photometry.

As a second test we use sources from the GOODS-S spectroscopic catalogs described in Section 2.1 within the redshift range $z = 3.0$–3.8, where both the 3.6 μm and 4.5 μm bands are uncontaminated by line flux from strong emission lines. We perform the exact same steps as described for our $z = 3.8$–5.0 spectroscopic galaxy sample in deriving the difference between the 3.6 μm photometry and the predicted continuum flux from the SED fitting. While any major systematics in our photometry would result in a median offset between the two, we find only a minor negative offset ($\Delta[3.6] = -0.02 \pm 0.01$ dex)s, indicating that, if anything, the Hα fluxes we derive are underestimated with respect to

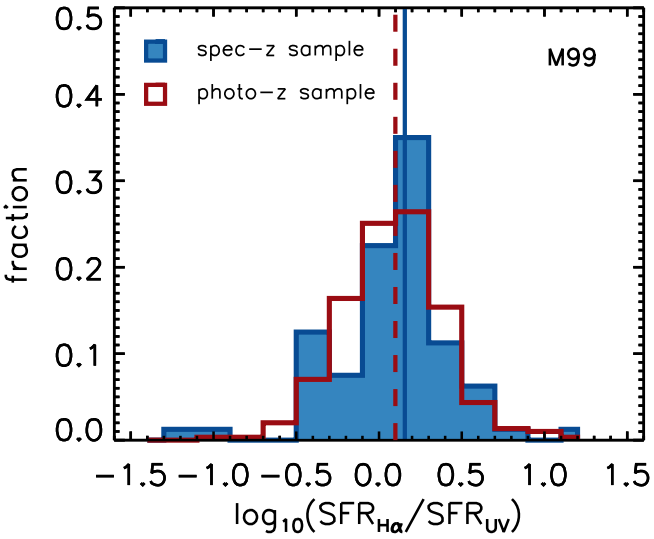

Figure 6. Histogram of star formation rates from the inferred Hα luminosities vs. those from the UV-luminosity corrected for dust using the UV slope β and the Meurer et al. (1999) calibration for the spectroscopic sample (blue filled histogram) and photometric-redshift-selected sample (red histogram).

their true value and therefore the discrepancy between $SFR_{UV+\beta}$ and $SFR_{H\alpha}$ can only increase.

Another systematic we need to consider is the influence of [O II] on the K-band flux for the fraction of sources in the redshift range $z = 4.35$–5.0. When we exclude the K_s-band photometry from the SED-fitting for galaxies from the spectroscopic sample in this redshift range, these sources have higher Hα+[N II]+[S II] EW by 0.05 dex. However, we find only a 0.002 dex difference in the median Hα+[N II]+[S II] EW of the total sample when specifically excluding the K_s band for the $z = 4.35$–5.0 sources. However, we note again that the systematic influence of [O II] can only increase the differences we see between $SFR_{UV+\beta}$ and $SFR_{H\alpha}$; it cannot resolve the discrepancy.

The discrepancy between $SFR_{UV+\beta}$ and $SFR_{H\alpha}$ was already noted by Shim et al. (2011), who found a mean $\langle SFR_{H\alpha}/SFR_{UV}\rangle \sim 6$, assuming no dust correction. This is significantly higher than the $SFR_{H\alpha}/SFR_{UV} \sim 2.1$ we find from our sample before dust correction. However the Shim et al. (2011) Hα emitter sample is IRAC-excess selected and could therefore be biased toward high inferred Hα EWs.

5. RECONCILING Hα AND UV-CONTINUUM-BASED SFRS

In this section, we discuss how the physical assumptions we make regarding the dust law, the star formation histories, and also ionizing photon production efficiencies of $z \sim 4$ star-forming galaxies affect the SFRs we derive from Hα and UV-continuum emission. As we demonstrated in the previous section, the use of relatively standard assumptions (the Calzetti et al. (2000) dust law and $A_{V,stars} = A_{V,gas}$) results in a systematic $\sim$−0.10–0.16 dex offset between Hα-based SFRs and UV-based SFRs.

5.1. Dust Law

In the previous section, we showed that UV and Hα-based SFR indicators are strongly correlated, though somewhat systemically offset ($\sim$0.15 dex) from a one-to-one relation, when using a Meurer et al. (1999) dust correction and assuming the same level of dust extinction for nebular light as stellar light (i.e., $A_{V,stars} = A_{V,gas}$).

Recently, the possibility of a different dust calibration for high-redshift sources was discussed by Dayal & Ferrara (2012), Wilkins et al. (2012, 2013a), de Barros et al. (2014), and Castellano et al. (2014). These authors argue that high-redshift sources likely have lower metallicities and younger ages than the local starburst galaxies used in the empirical Meurer et al. (1999) calibration. The Meurer et al. (1999) calibration implicitly assumes a dust-free UV-continuum slope of the galaxy of $\beta_{int} = -2.23$, consistent with solar metallicity and ages of a few hundred Myr. However, our $z \sim 4$ UV selected galaxies likely have ages around $\sim$100 Myr or less (see Section 3.1), while their metallicity content is expected to be no higher than 0.1–0.5 $Z_\odot$, measured for $z \sim 3$ UV selected galaxies by, e.g., Maiolino et al. (2008), Mannucci et al. (2009), and Troncoso et al. (2014). These physical properties result in bluer intrinsic UV-continuum slopes and therefore the dust reddening of the UV-continuum slope could be underestimated when assuming the Meurer et al. (1999) calibration.

Following the arguments above, the systemic offset between UV and Hα based SFR indicators in our $z \sim 4$ sample can be explained by an underestimate of our dust-correction due to the implicit assumption of $\beta_{int} = -2.23$. We investigate this possibility by considering a general dust correction of

$$A_{1600} = 1.99\,(\beta - \beta_{int}). \quad (4)$$

We vary the intrinsic UV-continuum slope, β_{int}, to recover a median $SFR_{H\alpha}/SFR_{UV+\beta} \sim 1$ after dust correction. Using this method we derive $\beta_{int} = -2.50^{+0.15}_{-0.06}$ for our spectroscopic sample and $\beta_{int} = -2.42^{+0.02}_{-0.06}$ for our photometric-redshift sample with the bootstrapping uncertainties. These values correspond to an age of $\sim$80 Myr, given a constant SFH and metallicity $Z = 0.5\,Z_\odot$. This is somewhat redder than the intrinsic slope of $\beta_{int} \sim -2.67$ found by Castellano et al. (2014), but similar to the range of β_{int} found by de Barros et al. (2014). Both of these values are derived from SED fitting. Furthermore simulations by Dayal & Ferrara (2012) and Wilkins et al. (2012, 2013a) suggest $\beta_{int} \sim -2.4$, which is slightly redder than our derived value.

To assess possible scenarios where the high-Hα SFRs with respect to UV-based SFRs are a result of bluer intrinsic UV-continuum slopes compared to the Meurer et al. (1999) relation, we compare our derived dust correction above with new far-infrared (FIR) and submillimeter constraints from the *Herschel* Space Telescope, Submillimeter Common-User Bolometric Array 2 (SCUBA2), the Atacama Large Millimetre Array (ALMA), and the Plateau de Bure Interferometer (PdBI) in Figure 7. While stacking analyses of $z \sim 2$ galaxy populations generally find good agreement with the Meurer et al. (1999) relation (e.g., Reddy et al. 2012; Oteo 2014; Pannella et al. 2015), recent measurements at even higher redshifts have reported conflicting results. Coppin et al. (2015) stack large samples of UV-selected galaxies at $z \sim 3$–5 using low-resolution data from *Herschel* and SCUBA2 and find consistent high dust content in the typical galaxy (left panel of Figure 7). Furthermore, Bourne et al. (2016) find a slope of 1.8 (as opposed to 1.99) and a $\beta_{int} \sim -2.22$ using stacked *Herschel* and SCUBA-2 imaging of galaxies 10^9–$10^{10}\,M_\odot$ and

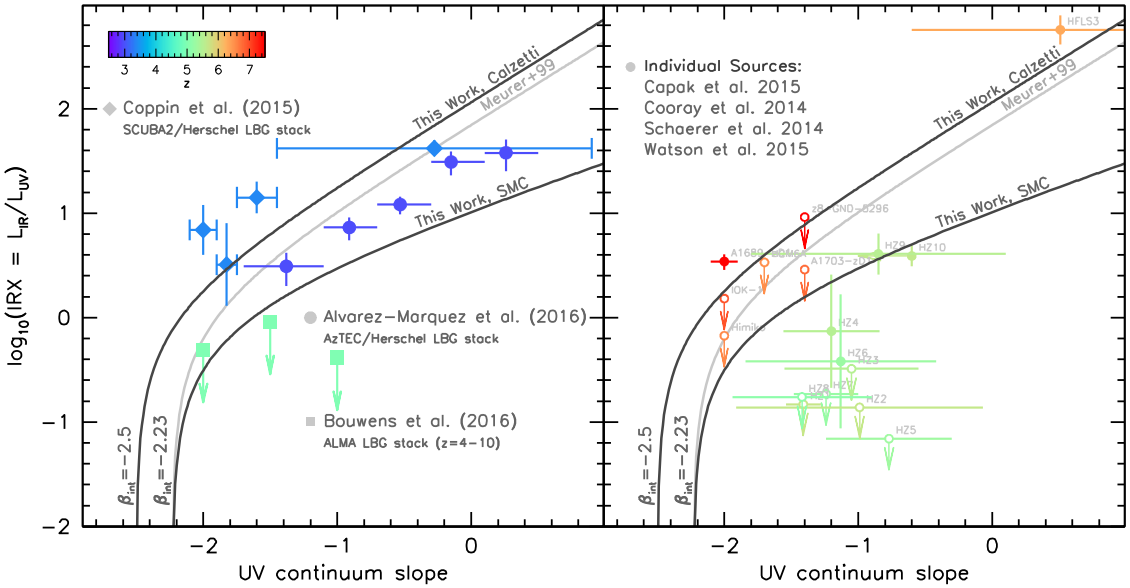

Figure 7. Current observational constraints on the IR-to-UV luminosity ratio as a function of the UV continuum slope (β) using stacks of UV-selected galaxies (left panel) and constraints on individual galaxies from ALMA and PdBI (right panel). While the stacking results by Coppin et al. (2015) over the redshift range $z \sim 3$–5 are in good agreement with the dust calibration needed to bring Hα- and UV-based SFR measurements, i.e., $A_{1600} = 1.99\,(\beta + 2.5)$ (see Section 5.1), many of the results suggest lower dust corrections (Cooray et al. 2014; Capak et al. 2015; Schaerer et al. 2015; Watson et al. 2015; Álvarez-Márquez et al. 2016; Bouwens et al. 2016a). At present, the impact that dust has on the observed UV brightness and SFRs of $z \sim 4$–5 galaxies is not clear, on the basis of far-IR observations.

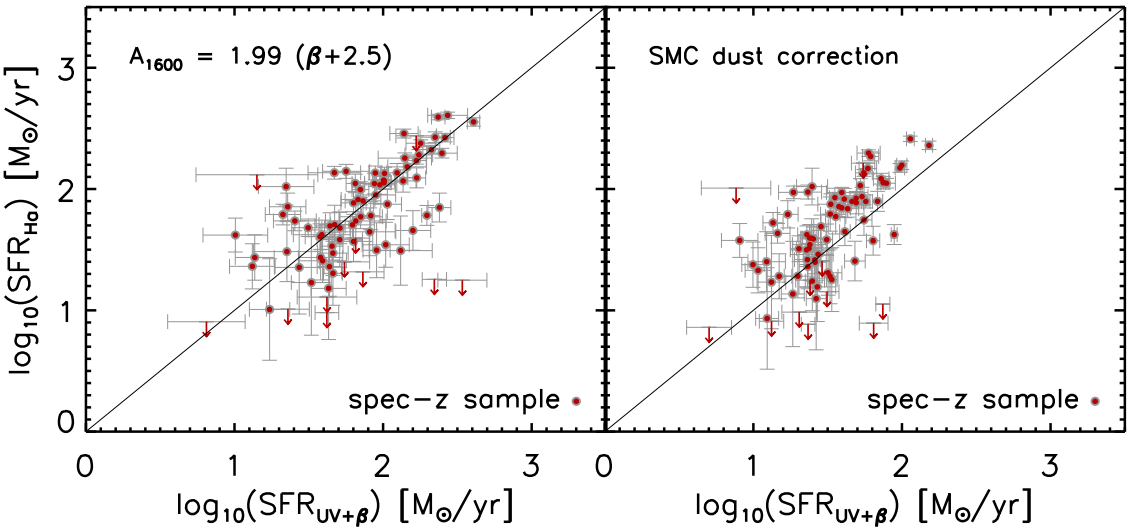

Figure 8. $\mathrm{SFR_{H\alpha}}$ as a function of $\mathrm{SFR_{UV+\beta}}$, using a dust correction calibrated to reproduce a median $\mathrm{SFR_{H\alpha}/SFR_{UV}} \sim 1$ (left panel, see Section 5.1) and the same figure assuming an SMC-type dust correction (right panel) for our spectroscopic sample; Hα is corrected for dust assuming $A_{V,\mathrm{stars}} = A_{V,\mathrm{gas}}$ and using the Calzetti et al. (2000) and SMC (Prevot et al. 1984) dust curve in the left and right panel, respectively. The direct calibration of different SFRs at $z \sim 4$ will be improved in the near future with large samples of galaxies with sensitive high-resolution dust continuum measurements from ALMA or PdBI.

$z = 0.5$–6, closely resembling the Meurer et al. (1999) relationship.

On the other hand the first small samples of high-resolution individual dust continuum detections and constraints on UV-selected $z \gtrsim 4$ galaxies (e.g., Capak et al. 2015; Schaerer et al. 2015; Knudsen et al. 2016) indicate a typical dust content significantly below the Meurer et al. (1999) relation (right panel of Figure 7). Indeed, recent stacking analyses of ALMA observations of low-mass galaxies in the Hubble Ultra Deep Field (Aravena et al. 2016; Bouwens et al. 2016a; Dunlop et al. 2016) indicate that sources below $10^{10}\,M_\odot$ show surprisingly faint infrared luminosities. In particular, comparing the low infrared excess as a function the UV-continuum slope in a sample of stacked galaxies below a stellar mass of $10^{9.75}\,M_\odot$, Bouwens et al. (2016b) find that the slope of the IRX-β relationship has to be <1.22 and <0.97 for $z \sim 2$–3 and $z \sim 4$–10 galaxies, respectively (Figure 7).

In conclusion, the first high-resolution FIR/submm observations taken by ALMA would indicate that the dust attenuation law is closer to that found for the Small Magellanic Cloud (SMC; e.g., Prevot et al. 1984). Oesch et al. (2013) show that an SMC-type dust-law is also preferred by the relationship between the UV-continuum slope and the colors (from UV to optical) of $z \sim 4$ galaxies.

The ambiguity in the dust correction of typical high-redshift UV-selected galaxies outlined in Figure 7 has significant implications for the interpretation of the high-Hα EWs and Hα SFRs derived in this work. In Figure 8 we show the Hα- and

UV-based SFRs, after applying two different dust corrections. The first (left panel) adopts a $A_{1600} = 1.99\,(\beta + 2.5)$ prescription. By construction, this produces an excellent match between Hα- and UV-based SFRs (and assumes an intrinsic UV-continuum slope $\beta_{\rm int} = -2.5$). In this case, the high-EW nebular emission lines found in high-redshift galaxies are in part the result of relatively high levels of dust-obscured star formation in combination with a similar dust attenuation between stars and the nebular light.

The right panel in Figure 8 uses

$$A_{1600} = 1.1\,(\beta + 2.23), \quad (5)$$

corresponding to a SMC-type dust correction for an intrinsic UV-continuum slope $\beta_{\rm int} = -2.23$, similar to that implicitly assumed for the Meurer et al. (1999) relation. We find a linear slope 1.1 from the tabulated extinction values of the SMC by Prevot et al. (1984). The resulting low levels of dust obscuration imply that, even for similar levels of attenuation between nebular and stellar light, the Hα SFRs are $0.19^{+0.02}_{-0.02}$ dex in the spectroscopic and $0.17^{+0.02}_{-0.03}$ dex in the photometric-redshift sample above what we would expect for the total amount of star formation derived from the dust-corrected UV light. While the samples of individual galaxies with high-resolution and high signal-to-noise constraints on the FIR light are still small, these results have significant consequences if correct. This provides us with the motivation to explore other mechanisms for recovering high $\rm SFR_{H\alpha}/SFR_{UV+\beta}$ ratios.

5.2. Star Formation Histories

In the previous section we investigated the effect of different dust calibrations on the $\rm SFR_{H\alpha}/SFR_{UV+\beta}$ ratio of $z \sim 4$ UV-selected galaxy samples. While it is possible to reconcile Hα- and UV-based SFR estimates by using the Kennicutt (1998) relations and assuming $A_{V,\rm stars} = A_{V,\rm gas}$ and dust corrections slightly above the values predicted by the Meurer et al. (1999) relation, it is not clear that such a dust law is supported by the observations of $z \geqslant 4$ galaxies.

The first direct high-resolution dust-continuum measurements of UV-selected high-redshift galaxies suggest that the typical dust content of these galaxies is significantly lower than this (see Figure 7). If future observations give similar results—implying more of an SMC dust law—our estimated SFRs using Hα would be systematically higher than when using the UV light. Here, we investigate how different star formation histories can play a role in the derived SFRs when using the locally derived Kennicutt (1998) relations.

5.2.1. Bursty Star Formation Histories

One possible explanation for the high $\rm SFR_{H\alpha}/SFR_{UV+\beta}$ ratios we derive in Section 4.1 is that the galaxies we examine are all predominantly young, i.e., that the Hα-based SFRs are much larger than UV-based SFRs (which saturate at ~100 Myr). However, it is possible that these galaxies are much younger, or perhaps that galaxies undergo regular bursts of star formation (e.g., Domínguez et al. 2015) which would give them the appearance of very young systems. This would boost the Hα flux, which is predominantly generated by short-lived (<10 Myr) O stars, with respect to the observed UV light, which is produced by O and B stars on a somewhat longer timescale (~100 Myr). This is the hypothesis that Shim et al. (2011) favor to explain the high $\rm SFR_{H\alpha}/SFR_{UV}$ in the sample they observe.

In Figure 5 we show $\rm SFR_{H\alpha}$ as a function of $\rm SFR_{UV+\beta}$ for both our spectroscopic sample (left) and our photometric sample (right). Since the majority of the sources in the left panel show Lyα in emission, one might suppose this population of sources could be biased toward starbursting systems relative to samples that are photometric-redshift-selected. However, we find little difference in the median $\rm SFR_{H\alpha}/SFR_{UV+\beta}$ ratio of our spectroscopic and our photometric sample. Moreover, a subsample of sources with stellar masses above our mass completeness limit of $\sim 10^{10}\,M_\odot$ gives a comparable median $\rm SFR_{H\alpha}/SFR_{UV+\beta}$ ratio to that of the entire photometric sample. These findings argue against supposing that very young (<10 Myr) starburst ages drive the systematic offsets we observe between Hα and UV SFRs.

To gain further insight we show the *specific* $\rm SFR_{H\alpha}$ as a function of the specific $\rm SFR_{UV+\beta}$ in Figure 9, again assuming a Meurer et al. (1999) dust law and $A_{V,\rm stars} = A_{V,\rm gas}$. The two sSFR estimates correlate strongly over ~2 dex in sSFR and we find a constant offset between the Hα and UV probes of ~0.15 dex. For young galaxies that are formed in a single burst of star formation, we would expect the discrepancy between $\rm sSFR_{H\alpha}$ and $\rm sSFR_{UV+\beta}$ to decrease with decreasing $\rm sSFR_{H\alpha}$. For reference we include a single stellar population (SSP) track (pink line) that demonstrates the rapid evolution of the $\rm sSFR_{H\alpha}/sSFR_{UV+\beta}$ ratio of this stellar population with age. A burst of star formation is expected to show enhanced Hα for ~5 Myr, but we would expect many sources with ages >10 Myr after the burst below the one-to-one relation. Comparing this model with our observations, we see no clear trend in favor of young ages.

To test this scenario further we run a Monte Carlo simulation, which we consider a population of galaxies with bursty star formation histories. To reproduce the properties in our sample we randomly draw from the distribution of derived stellar masses for our observed galaxy sample and populate each galaxy with bursts of mass $M_{\rm burst}$ distributed linearly in time with a typical time interval $\rm dt_{burst}$. For each burst we add an SSP model obtained from the Starburst99 models (Leitherer et al. 1999) with the corresponding age to the total SED of the simulated source. We derive $\rm SFR_{UV}$ and $\rm SFR_{H\alpha}$ from the final SED using the Kennicutt (1998) relations. Because our observed galaxy sample is limited by the H_{160} band flux, we assume that the galaxy population can be modeled as an $\rm SFR_{UV}$-limited sample (assuming $\rm SFR_{UV}$ scales linearly with $L_{\rm UV}$ through Equation (1)). Therefore, we impose a $\rm SFR_{UV}$ lower limit on our simulated galaxy population of 5 $M_\odot$ yr^{-1}. We assign observational errors to the simulated data points, using the observed uncertainties in the derived SFRs. Using these simulations we investigate what parameters of $M_{\rm burst}$ and $\rm dt_{burst}$ can roughly reproduce a galaxy population with a similarly high $\rm SFR_{H\alpha}/SFR_{UV+\beta}$ ratio when assuming the Kennicutt (1998) relations as the typical source in our observed galaxy samples.

Figure 10 shows two such simulations that produce a large number of sources with $\rm SFR_{H\alpha}/SFR_{UV+\beta} > 1$. To reproduce the observed galaxy distribution we find that we typically need high burst masses of $M_{\rm burst} \sim 10^8\,M_\odot$ to reproduce the generally high sSFRs, and reasonably short burst intervals of $\rm dt_{burst} \sim$ 5–10Myr to generate high Hα fluxes. While roughly half of the galaxies in our simulation have $\rm SFR_{H\alpha}/SFR_{UV+\beta} > 1$, our

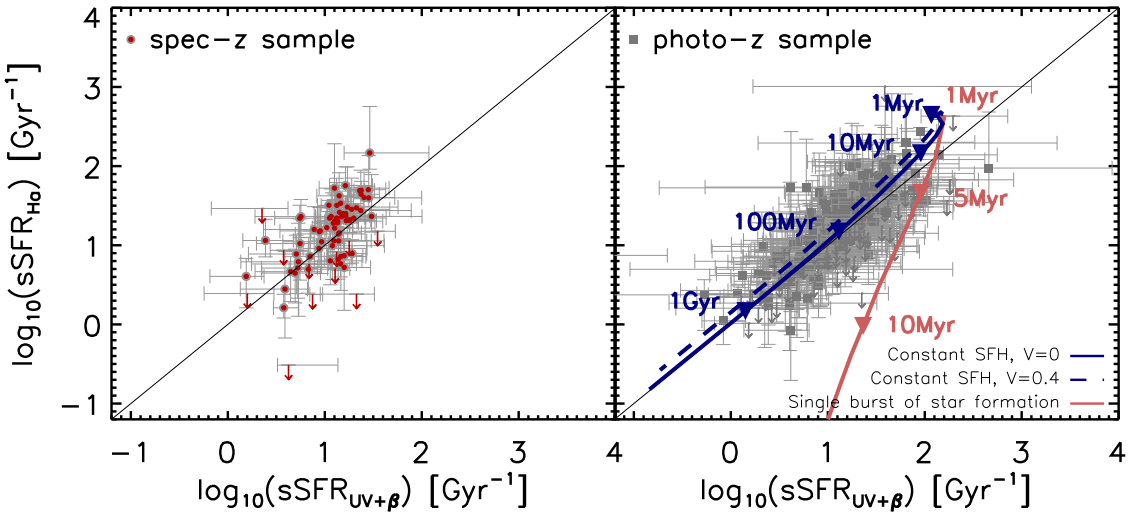

Figure 9. Specific star formation rates from the inferred Hα luminosities vs. those from the UV-luminosity corrected for dust using the UV slope β and the Meurer et al. (1999) calibration (red points; red arrows indicate the 1σ upper limits); Hα is corrected for dust assuming $A_{V,\rm stars} = A_{V,\rm gas}$ and using the Calzetti et al. (2000) dust curve. The left panel shows our spectroscopic sample, while the right panel shows our photometric sample. The right panel includes two stellar population Starburst99 models from Leitherer et al. (1999). The pink track includes only single-star populations and follows a single burst of star formation with an initial mass of $10^6\,M_\odot$. We indicate the measured sSFRs of this model using the Kennicutt (1998) relations at ages of 1 Myr, 5 Myr, and 10 Myr (pink triangles). The dark blue tracks indicate stellar populations with a constant star formation history of 1 $M_\odot$ yr^{-1}, where the solid line indicates a stellar population with no rotation ($V = 0$) and the dashed line indicates a stellar population with rotation levels at 40% of the break-up velocity ($V = 0.4$ Leitherer et al. 2014). We indicate the measured sSFRs of this model using the Kennicutt (1998) relations at ages of 1 Myr, 10 Myr, 100 Myr, and 1 Gyr (dark blue triangles). The one-to-one relation in the sSFRs favors a relatively smooth star formation history, given the fact that very few sources are at low $\rm sSFR_{H\alpha}$ as would be the case for a starburst with an age of >10 Myr.

simulations also show a rather large tail of relatively low-Hα sSFR galaxies, i.e., ~53% of the simulated galaxy distributions in the left panel of Figure 10 have $\rm sSFR_{H\alpha} < 2\ yr^{-1}$. This is in contrast to the observed galaxies in our large photometric sample where ~26% of the sources have upper limits in $\rm SFR_{H\alpha}$ and could therefore populate this low-sSFR tail.

In conclusion, we find that bursty star formation histories predict at least twice as many galaxies with $\rm sSFR_{H\alpha} < 2\ yr^{-1}$ as are seen in the observations. The implication is that the star formation histories of galaxies are considerably smoother than those in the toy model we consider above and that bursty star formation histories do not provide a resolution for the tension between the Hα- and UV-based SFRs. These results are in agreement with simulated star formation histories that predict that burstiness is mostly present in low-mass ($\lesssim 10^8\,M_\odot$) galaxies (e.g., Dayal et al. 2013; Sparre et al. 2015).

5.2.2. Rising Star Formation Histories

In Section 5.2.1 we describe how the distribution of Hα- and UV-based sSFRs disfavors bursty star formation histories. However, a smoothly rising SFH can also affect the $\rm SFR_{H\alpha}/SFR_{UV+\beta}$ ratio simply because the UV flux probes the time-averaged SFR over a ~100 Myr time window. As the SFR for rising star formation histories is lower at earlier times in a ~100 Myr time window, the SFR inferred from the UV light would be lower than the instantaneous SFR.

Reddy et al. (2012) tabulate the values of $\rm SFR/L_{1700}$ as a function of galaxy age for different star formation histories (see their Table 6). Using their tabulated values, an exponentially rising star formation history ($\tau \sim 100$) results in a ~0.07 dex higher $\rm SFR/L_{1700}$ ratio for a galaxy of 100 Myr compared to a constant SFH. Assuming that Hα is a good tracer of the instantaneous SFR, we estimate that rising star formation histories can reasonably result in a ~0.1 dex offset $\rm SFR_{H\alpha}/SFR_{UV+\beta}$ ratio.

Similar to the scenario of bursty star formation histories, rising star formation histories can work well in combination with a Meurer et al. (1999) dust correction to explain the values of $\rm SFR_{H\alpha}$ and $\rm SFR_{UV+\beta}$ in our $z \sim 4$ galaxy sample. However, if these galaxies prefer a SMC-type dust correction such as suggested by e.g., Capak et al. (2015), the offset in the derived $\rm SFR_{H\alpha}/SFR_{UV+\beta}$ values cannot be explained by just invoking rising star formation histories.

5.3. Production Efficiency of Ionizing Photons

In Section 5.2 we discussed the impact of the assumed star formation history on the offset derived from Hα-and UV-based SFR indicators in our $z \sim 4$ galaxy sample. While bursty or rising star formation histories will produce a ~0.1-dex systematic offset between the two SFR indicators, this does not resolve the tension between these two SFR measures adopting an SMC dust law (where there is a ~0.2-dex offset: see Figure 8 and Table 3).

Another effect on the $\rm SFR_{H\alpha}/SFR_{UV+\beta}$ ratio that we must consider is the potential for a changing conversion factor between $L_{\rm H\alpha}$ and SFR (i.e., Equation (3), see also Zeimann et al. 2014). While the Hα flux scales directly with the number of ionizing photons emerging from the H II regions in the galaxy (Leitherer & Heckman 1995; Kennicutt 1998), the shape of the ionizing spectrum in low-metallicity galaxies is poorly constrained. In particular the impact of massive binaries (e.g., de Mink et al. 2009; Sana et al. 2012), rotational mixing (e.g., Ramírez-Agudelo et al. 2013), and line blanketing can change with metallicity. For a more elaborate discussion we refer to Section 3 in Kewley et al. (2013) and the discussion in Steidel et al. (2014). Furthermore, differences in the high-mass slope of the IMF would also introduce a different ionizing spectrum. Even without changes in the IMF, a metallicity-dependent ionizing spectrum could significantly affect the $\rm SFR_{H\alpha}/SFR_{UV+\beta}$ ratio. If stars in high-redshift galaxies are

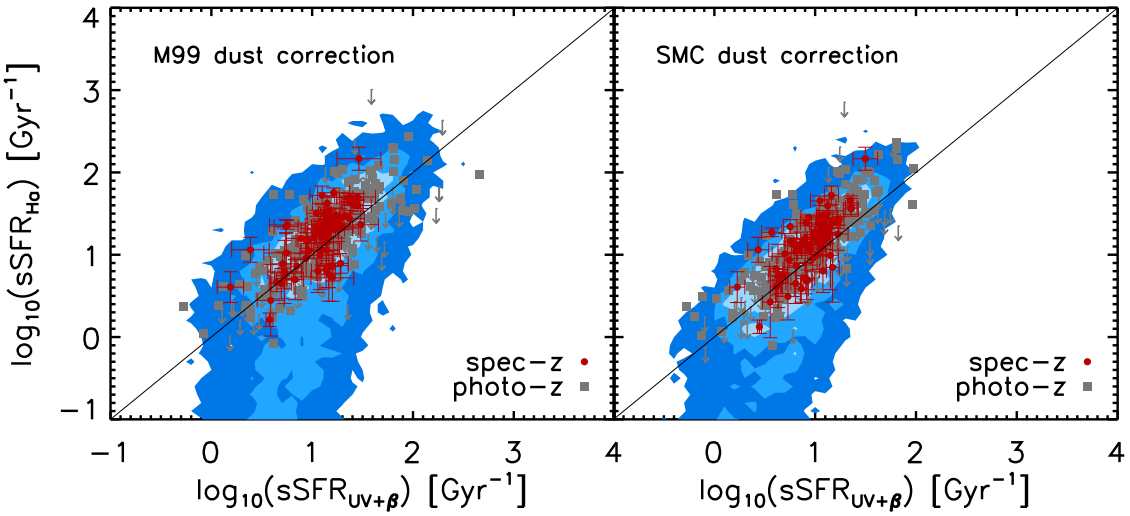

Figure 10. Specific star formation rates from the inferred Hα luminosities vs. those from the UV-luminosity corrected for dust using the UV slope β and the Meurer et al. (1999) calibration (left panel) or a SMC-type calibration (right panel); Hα is corrected for dust assuming $A_{V,\rm stars} = A_{V,\rm gas}$ and using the Calzetti et al. (2000) and SMC (Prevot et al. 1984) dust curve in the left and right panel, respectively. Data points indicate the observed spectroscopic (red points) and photometric-redshift-selected (gray squares) samples. The blue contours show a simulated galaxy distribution with masses and specific star formation rates that are largely similar to our observed galaxy samples, assuming a bursty star formation history with burst masses $M_{\rm burst} \sim 10^8\,M_\odot$ and burst intervals of $dt_{\rm burst} \sim 5$–$10 Myr$ (see Section 5.2.1). The simulations are cut below $\rm SFR_{UV} < 5\,M_\odot\,yr^{-1}$ to mirror the UV-selection of the observed sample. Post-starburst galaxies are visible in the UV for ∼100 Myr, while Hα probes the instantaneous SFR. The fraction of sources in the resulting low $\rm sSFR_{H\alpha}$ tail is twice as large in the simulated distribution as that found in the observed sample (including upper limits).

really much more efficient producers of ionizing photons, this would significantly impact galaxies' possible role in reionizing the universe (Bouwens et al. 2016b; Stark et al. 2015, 2016).

We illustrate this in the right panel of Figure 9, where we show stellar population tracks for a constant star formation history for stars with zero rotation (at solar metallicity) and for stars that rotate at 40% of the break-up velocity (at $Z = 0.6\,Z_\odot$) from the models described in Leitherer et al. (2014). At 100 Myr, the low-metallicity models that include stellar rotation are ∼0.15 dex offset in the $\rm SFR_{H\alpha}/SFR_{UV+\beta}$ ratio compared to the model that does not include stellar rotation.

A similar effect is seen when using the Eldridge & Stanway (2012) models that include binary star evolution. Comparing their models that include binaries at $Z = 0.2\,Z_\odot$ with the model for single-star evolution at solar metallicity we find a ∼0.31 dex offset in the $\rm SFR_{H\alpha}/SFR_{UV+\beta}$ ratio, arising from a ∼0.46 dex offset in Hα flux and ∼0.15 dex in UV luminosity.

Possible evolution in the SFR-$L_{\rm H\alpha}$ relationship therefore offers us a way to explain the observed high Hα fluxes even in the scenario where the typical high-refshift UV-selected galaxy has low dust masses, as has been argued by Schaerer et al. (2015) and Capak et al. (2015).

In Table 3 we give an overview of how each of the models considered in this section impacts the $\rm SFR_{H\alpha}/SFR_{UV+\beta}$ ratios. Over the next few years, ALMA will likely shed light on the typical dust properties of $z \sim 4$ galaxies, and as a result will provide us with new insights into the star formation histories and ionizing spectra of high-redshift galaxies.

6. IMPLICATIONS

In the previous section, we considered a variety of different physical mechanisms for reconciling current measures of the SFRs as derived from Hα or from UV-continuum light.

On the basis of this discussion (and comparison with the observations), we find that there are at least two flavors of physical models that appear to be plausible. The first supposes that $z \sim 4$ galaxies can be described using a Meurer et al. (1999) dust calibration with $A_{V,\rm stars} = A_{V,\rm gas}$ and that the UV-based SFR estimates need to be corrected by ∼0.1 dex to correct the measured, time-averaged values to the instantaneous ones. The second supposes that $z \sim 4$ galaxies can be described using an SMC dust calibration with $A_{V,\rm stars} = A_{V,\rm gas}$ and that $z \sim 4$ galaxies are more efficient at producing ionizing photons than galaxies in standard stellar population models (and thus the $L_{\rm H\alpha}$/SFR ratio is high; see Bouwens et al. 2016b; and Stark et al. 2015, 2016 for a discussion of how this may affect the galaxies' role in driving the reionization of the universe).

These two scenarios are summarized in Table 4. Which of these scenarios is the relevant one largely hinges on the dust law (see Figure 7) and should be resolved definitively in the near future with deeper ALMA data and larger samples of indiviual detections of high-redshift galaxies. Given that the current ALMA results of both indiviually detected UV-bright galaxies (e.g., Capak et al. 2015) and large samples of faint stacked galaxies (e.g., Bouwens et al. 2016a) indicate a signficantly lower infrared excess for low-mass high-redshift galaxies than predicted by the Meurer et al. (1999) calibration, we will assume for the remainder of this section that the latter scenario, assuming a SMC-type dust calibration, provides a reasonable basis from which to derive new results on the SFR-stellar mass relation and also the $z = 4$–8 SFR functions. However, we will also look at the results assuming the former scenario involving the Meurer et al. (1999) dust law to be the correct one in Appendix B.

6.1. SFR-stellar Mass Sequence

One of the most fundamental relations for understanding galaxy build-up is the SFR-stellar mass relation, or the main sequence of star-forming galaxies. Using our derived Hα-based SFRs we are in an excellent position to assess this relation at $z \sim 4$, given the much weaker sensitivity of our Hα-

Table 3
Quantitative Considerations in Achieving Consistent $SFR_{H\alpha}$ and SFR_{UV} Measurements

Assumed dust correction	Consistency of SFRs for dust model		
	$\log_{10}(SFR_{H\alpha}/SFR_{UV})$[a]	$0.4A_{H\alpha}$[b]	$0.4A_{UV}$[b]
None[c]	$0.35^{+0.04}_{-0.05}$	0.00	0.00
Meurer+99, $A_{V,stars} = A_{V,gas}$[c]	$0.16^{+0.02}_{-0.04}$	0.12	0.35
Meurer+99, $A_{V,stars} = 0.44 \cdot A_{V,gas}$[c]	$0.28^{+0.02}_{-0.01}$	0.27	0.35
SMC dust correction, $A_{V,stars} = A_{V,gas}$[d]	$0.19^{+0.02}_{-0.02}$	0.04	0.19
$A_{1600} = 1.99(\beta + 2.54)$, $A_{V,stars} = A_{V,gas}$[d]	$0.01^{+0.03}_{-0.04}$	0.19	0.57
Other Physical Assumptions that Impact the Consistency of SFRs			
Assumed properties of stars/SF history	$\Delta \log_{10}(SFR_{H\alpha}/SFR_{UV})$[h]	$\Delta \log_{10}(SFR_{H\alpha})$[h]	$\Delta \log_{10}(SFR_{UV})$[h]
Rising SFH (Reddy+2012)[e,g]	+0.07	+0.00	−0.07
Stellar rotation (Leitherer+2014)[f,g]	+0.14	+0.24	+0.10
Stellar binaries (Eldridge & Stanway 2012)[f,g]	+0.31	+0.46	+0.15

Notes.
[a] Measured median values and bootstrapping uncertainties are based on the spectroscopic sample. The measured values are somewhat lower than those derived by Shim et al. (2011), who find $\log_{10}(SFR_{H\alpha}/SFR_{UV}) \sim 0.78$ dex when applying no dust correction, but in good agreement with the sSFRs found by Stark et al. (2013) and Mármol-Queraltó et al. (2016), who assume Meurer et al. (1999) dust corrections.
[b] Median estimated extinction (dex) in the UV-continuum (1600 Å) and Hα line.
[c] See Section 4.1.
[d] See Section 5.1.
[e] See Section 5.2.2.
[f] See Section 5.3.
[g] Determined for a stellar population with an age of 100 Myr.
[h] Value of the inferred SFRs (and SFR ratios) using the Kennicutt (1998) relations minus the actual SFRs. If the value in the table is positive, SFRs (or SFR ratios) estimated from the observations (Hα or UV light) using the Kennicutt (1998) relations will be overestimated. If the value in the table is negative, SFRs estimated using the Kennicutt (1998) relations will be underestimated.

Table 4
Observationally Motivated Physical Assumptions (see Table 3) Used in Deriving Our Fiducial $z = 4$–8 SFR Functions and Star Formation Main Sequence Results at $z \sim 4.3$

Assumptions SFR functions	$\log_{10}(SFR_{H\alpha}/SFR_{UV})$[a]	$\Delta \log_{10}(SFR_{H\alpha})$[b]
Fiducial model	$-0.01^{+0.02}_{-0.02}$	−0.20
SMC dust correction, $A_{V,stars} = A_{V,gas}$	…	…
Stellar rotation (see Section 5.3 and Table 3)	…	…
Rising SFH (see Section 5.2.2 and Table 3)	…	…
(results presented in Section 6: Figures 11–12 and Tables 5–7)	…	…
Alternate fiducial model	$0.09^{+0.02}_{-0.04}$	+0.12
Meurer+99, $A_{V,stars} = A_{V,gas}$	…	…
Rising SFH (see Section 5.2.2 and Table 3)	…	…
(results presented in Appendix B: Tables 8–9)	…	…

Notes.
[a] Median ratio of the SFRs derived from Hα and the UV-continuum light making use of the assumptions in these observationally motivated physical models.
[b] Value of the inferred SFRs using the fiducial assumptions minus the SFRs derived using the Kennicutt (1998) relations with no dust corrections. SFRs calculated using our fiducial model assuming SMC extinction will be systematically 0.32 dex lower than SFRs in our alternate fiducial model with the Meurer et al. (1999) extinction.

based SFR measurements to many of the classic degeneracies that affect stellar population modeling (e.g., dust versus age). For this analysis we will make use of the Hα measurements corrected as described in Section 4 to obtain a good estimate of the instantaneous SFR. As specified at the beginning of this section, we utilize an SMC dust correction (Equation (5)) and $A_{V,stars} = A_{V,gas}$. As a result we have to conclude that a higher production efficiency of ionizing photons impact the $SFR_{H\alpha}/SFR_{UV+\beta}$ ratio and therefore we correct the Hα SFRs downward by 0.2 dex with respect to the values obtained with the Kennicutt (1998) relation (Equation (3)). See Table 3 to see what how other dust corrections would affect our final result.

In Figure 11 we show $SFR_{H\alpha}$ and $sSFR_{H\alpha}$ as a function of stellar mass for our spectroscopic and photometric samples. Since only sources with $H_{160,AB}$ magnitudes brighter than 26.5 (see Section 2.2) were included in our sample (equivalent to a SFR_{UV} limit of $\sim 4\,M_\odot\,yr^{-1}$), we present this selection limit very clearly in this figure. We find that a fit using only sources above $10^{9.8}\,M_\odot$ is consistent within the uncertainty with the unity low-mass slope as found by Whitaker et al. (2014) for star-forming galaxies between $z \sim 0.5$ and 2.5.

Furthermore, we estimate the scatter in the main sequence of star-forming galaxies from the Bayesian linear regression (solid line in the left panel of Figure 11) with a flat prior (Kelly 2007),

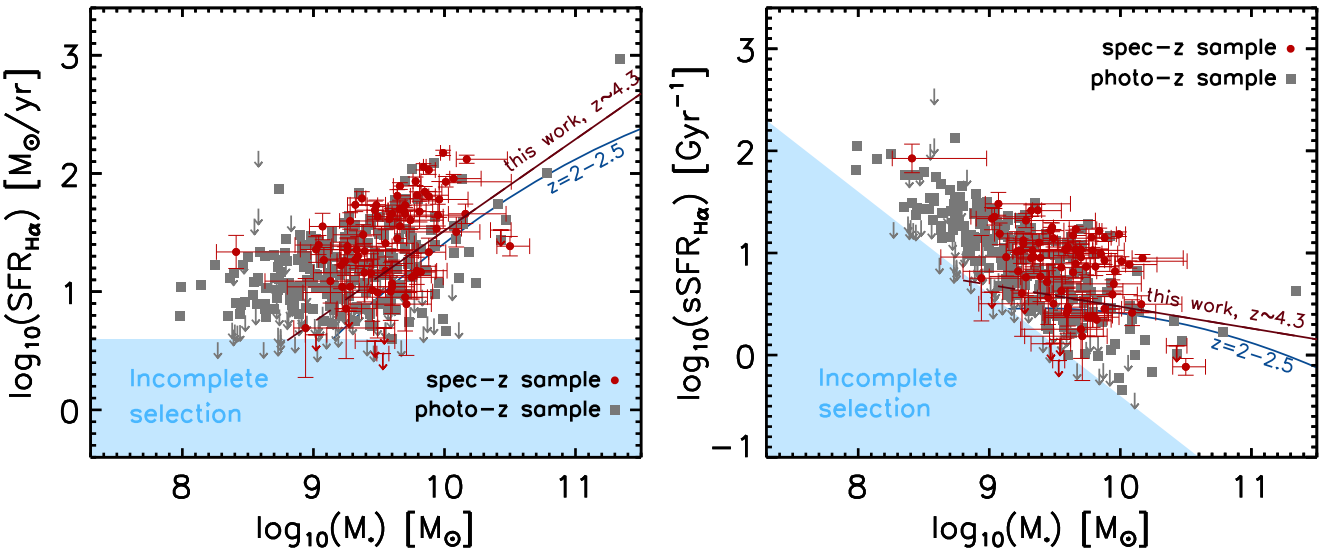

Figure 11. $SFR_{H\alpha}$ (left) and $sSFR_{H\alpha}$ (right) as a function of stellar mass for our spectroscopic (red points) and photometric (gray squares) sample, respectively. The solid red lines indicates the Bayesian linear regression for galaxies $M_* > 10^{9.5}\,M_\odot$, while the blue line indicates the polynomial derived by Whitaker et al. (2014) for $z = 2.0$–2.5 galaxies. The blue shaded region gives an indication of the incompleteness in our sample due to the UV selection. We find that the slope of the SFR-stellar mass sequence is broadly consistent with unity and an intrinsic scatter of $\lesssim$0.4 dex.

Table 5
Parameters of the $SFR_{H\alpha} - M_*$ Sequence

$d\log_{10}(\mathrm{SFR})/d\log_{10}(M_*)$	0.78 ± 0.23
$\log_{10}(\mathrm{SFR}_{H\alpha})_{M_*=10^{10}\,M_\odot}$ $[M_\odot/\mathrm{yr}^{-1}]$	1.51 ± 0.07
$\sigma_{\mathrm{intrinsic}}$	0.36 ± 0.06

Note.
Based on the Bayesian linear regression of all sources in our combined photometric and spectroscopic sample (sources that are present in both samples are only counted once) with $M_* > 10^{9.8}\,M_\odot$.

Table 6
Schechter Parameters of the SFR Functions: SMC Dust Correction

$\langle z \rangle$	$\log_{10}\frac{\mathrm{SFR}^*}{M_\odot\,\mathrm{yr}^{-1}}$	ϕ^*_{SFR} $(10^{-3}\,\mathrm{Mpc}^{-3})$	α_{SFR}
3.8	1.41 ± 0.04	$1.76^{+0.30}_{-0.26}$	-1.57 ± 0.06
4.9	1.53 ± 0.06	$0.65^{+0.16}_{-0.12}$	-1.66 ± 0.08
5.9	1.42 ± 0.10	$0.41^{+0.18}_{-0.13}$	-1.72 ± 0.16
6.8	1.37 ± 0.14	$0.27^{+0.18}_{-0.10}$	-1.82 ± 0.23
7.9	1.19 ± 0.24	$0.18^{+0.20}_{-0.10}$	-1.91 ± 0.41

Note.
These Schechter parameters are obtained following the procedure described by Smit et al. (2012). We assume an SMC dust correction (Equation (5)) and adopt the linear relation between the UV-continuum slope β and UV luminosity found by Bouwens et al. (2014) (see Section 6.2) and we assume the Kennicutt (1998) conversion from UV to SFR (Equation (1)).

which gives an intrinsic scatter of ∼0.4 dex, indicative of a modestly smooth star formation history. This intrinsic scatter is significantly higher than the ∼0.13 dex scatter measured by Speagle et al. (2014) based on the Shim et al. (2011) sample, but is in good agreement with the recent determination from Salmon et al. (2015).

While the dynamic range where we have a mass complete sample is limited, we can compare the normalization of our SFR-stellar mass sequence with determinations at lower redshift in more detail. At a stellar mass of $10^{10}\,M_\odot$ we find from our Bayesian fits $\log_{10}\mathrm{SFR}_{H\alpha}/M_\odot\,\mathrm{yr}^{-1} = 1.51 \pm 0.07$ and $\log_{10}\mathrm{sSFR}_{H\alpha}/\mathrm{Gyr}^{-1} = 0.47 \pm 0.06$ (uncertainties obtained through bootstrapping). This is slightly lower than the fit by Speagle et al. (2014), who compare 25 studies between $z \sim 0$ and $z \sim 6$ and predict an SFR of $\log_{10}\mathrm{SFR}/M_\odot\,\mathrm{yr}^{-1} \sim 1.73$ (corrected for differences in IMF) at our median redshift $\langle z_{\mathrm{spec}} \rangle = 4.25$ and stellar mass of $10^{10}\,M_\odot$. Furthermore, extrapolating the relation for $\mathrm{sSFR} \propto (1+\mathrm{z})^{1.9}$ found by Whitaker et al. (2014) between $z \sim 0.5$ and 2.5, we would predict $\log_{10}\mathrm{SFR}/M_\odot\,\mathrm{yr}^{-1} \sim 2.05$ at $10^{10}\,M_\odot$ if this relation held out to $z \sim 4$. The lower SFRs in comparison with these lower redshift extrapolations could indicate a flatter evolution of the main sequence of star-forming galaxies with redshifts above $z > 2$, such as suggested by González et al. (2014) and Mármol-Queraltó et al. (2016).

Comparing our normalization of the main sequence with recent estimates at the same redshift we find lower values than Stark et al. (2013) and Mármol-Queraltó et al. (2016), who find $\log_{10}\mathrm{sSFR}_{\mathrm{UV}+\beta}/\mathrm{Gyr}^{-1} \sim 0.79$ at $5 \cdot 10^9\,M_\odot$ and $\log_{10}\mathrm{sSFR}_{\mathrm{UV}+\beta}/\mathrm{Gyr}^{-1} \sim 0.73$ at $10^{10}\,M_\odot$, respectively. Although these authors use the same technique for deriving the Hα SFR, they assume a Meurer et al. (1999) dust correction, which explains the discrepancy. Our determinations are in good agreement with the results by González et al. (2014), who find $\log_{10}\mathrm{sSFR}_{\mathrm{SED}}/\mathrm{Gyr}^{-1} \sim 0.54$ at $5 \cdot 10^9\,M_\odot$ using sSFRs from SED fitting. On the other hand we find slightly higher values than two recent studies using SED fitting results: Duncan et al. (2014) find $\log_{10}\mathrm{sSFR}_{\mathrm{SED}}/\mathrm{Gyr}^{-1} \sim 0.37$ at $5 \cdot 10^9\,M_\odot$ and Salmon et al. (2015) find a median $\log_{10}\mathrm{SFR}_{\mathrm{SED}}/M_\odot\,\mathrm{yr}^{-1} \sim 1.35$ at $z \sim 4$ and $10^{10}\,M_\odot$ (approximately implying $\log_{10}\mathrm{sSFR}_{\mathrm{SED}}/\mathrm{Gyr}^{-1} \sim 0.35$). Differences between SFRs derived from SED fitting and Hα inferred SFRs could be due to the assumed SFH, the dust law and metallicity assumed in both methods, the age-dust degeneracy in the SED fitting, and the stellar library that is used for the SED fit; in particular, including binary and/or rotating stars changes the strength of the

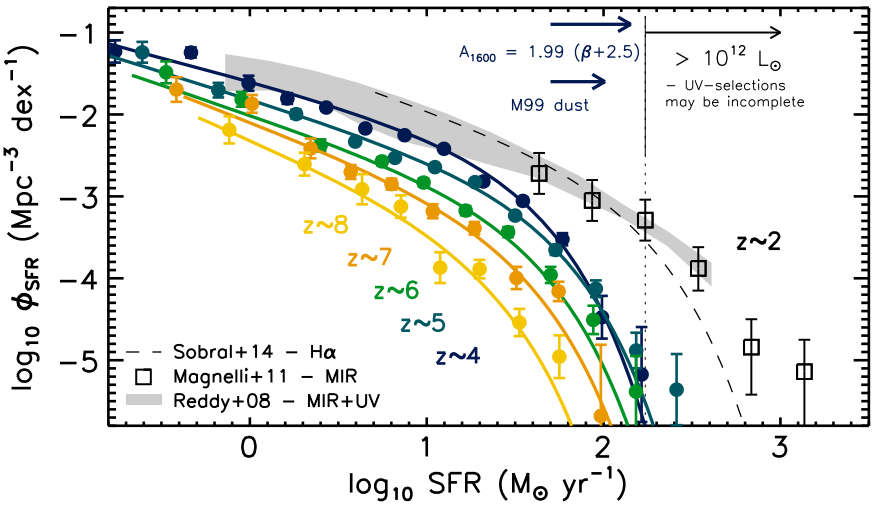

Figure 12. The $z = 4$–8 SFR functions derived here following the Smit et al. (2012) procedure. The SFR functions are based on the UV luminosity functions by Bouwens et al. (2015), the color–magnitude relations determined by Bouwens et al. (2014), and the SMC-type dust calibration (Equation (5)). We assume the Kennicutt (1998) conversion from UV to SFR (Equation (1)). Stepwise dust-corrected SFR functions (solid points) with the analytical solutions for the Schechter functions (see Equations (4), (7), and (8) in Smit et al. 2012). The black dotted line indicates the SFR range where the Bouwens et al. (2015) UV selection could be incomplete owing to dust saturation or where the dust corrections are inaccurate. The dark blue arrows indicate the change in the knee of the SFR function, assuming different dust corrections $A_{1600} = 1.99(\beta + 2.5)$ or $A_{1600} = 1.1(\beta + 2.23)$ and using the Kennicutt (1998) conversion from UV to SFR (see Section 5.1). For reference we include SFR functions at $z \sim 2$ from Hα (dashed black line; Sobral et al. 2014), MIR (open black squares; Magnelli et al. 2011), and UV+MIR (gray shaded region; Reddy et al. 2008) SFR probes.

Hα EW at a fixed galaxy age, which influences the SFR and sSFR fitting parameters obtained in the SED fitting.

We summarize our findings on the $\mathrm{SFR}_{\mathrm{H}\alpha} - M_*$ sequence in Table 5.

6.2. Star Formation Rate Functions

Another application of our improved measurements of the SFR at $z \sim 4$ using both UV continuum and $H\alpha$ information is the determination of the SFR functions (Smit et al. 2012) at $z = 4$–8. The SFR function is useful since it can be used to connect high-redshift UV-luminosity functions with Hα and infrared-based SFR functions at $z \sim 2$.

Smit et al. (2012) give a prescription to correct UV-luminosity functions for dust based on a luminosity-dependent determination of the UV slope, β (e.g., Bouwens et al. 2012, 2014); a dust calibration of the form $A_{1600} = C_0 + C_1\beta$; and a fixed scatter around the β-luminosity relation, σ_β (see Equations (4), (7), and (8) by Smit et al. 2012). We assume a low-metallicity stellar population including stellar rotation, as well as a rising SFH (see Table 4) and therefore convert the dust-corrected UV-luminosity functions to SFR functions using the Kennicutt (1998) relation (Equation (1)), with no correction, since the offsets due to the SFH and the higher production efficiency of ionizing photons roughly cancel each other out (see Table 3). At the same time, Equation (3) overpredicts $\mathrm{SFR}_{\mathrm{H}\alpha}$ by ~0.2 dex, explaining the high $\mathrm{SFR}_{\mathrm{H}\alpha}/\mathrm{SFR}_{\mathrm{UV}+\beta}$ ratio.

Stepwise determinations and Schechter paramters are given in Tables 7 and 6, respectively. We base our SFR functions on the determination of the UV-luminosity functions at $z \sim 4$–8 by Bouwens et al. (2015) and determination of the color–magnitude relations by Bouwens et al. (2014). The resulting SFR functions are shown in Figure 12 in combination with the Hα-based SFR function derived by Sobral et al. (2014), the UV+MIR luminosity function derived by Reddy et al. (2008), and the MIR luminosity function measured by Magnelli et al. (2011) converted to SFR using the Kennicutt (1998) relation.

In Figure 12, the SFR range above $\sim 150 M_\odot$ yr^{-1}, is equivalent to $L_{\mathrm{bol}} > 10^{12}\, M_\odot$, where we might expect dust saturated sources that are missed in an UV-selected sample. Given that the $z \sim 4$ and $z \sim 5$ SFR functions reach beyond $L_{\mathrm{bol}} > 10^{12}\, M_\odot$, we might imagine our SFR functions to be underestimated at the high end. Our results for the SFR function are fairly similar to those recently obtained by Mashian et al. (2016).

Instead of the SMC dust-correction, we could have assumed Meurer et al. (1999) extinction and explained the discrepancy of UV- and Hα based SFR estimates owing to a rising star formation history and therefore using a conversion factor 0.1 dex higher than the Kennicutt (1998) relation (Equation (1)) to match the instantaneous Hα SFR. The resulting knee of the $z \sim 4$ SFR function would shift by ~+0.3 dex. The individual bins and Schechter parameters derived using a Meurer et al. (1999) dust calibration are presented in Appendix B in Tables 8–9.

Alternatively we can assume $A_{1600} = 1.99(\beta + 2.5)$, derived in Section 5.1 (see Figure 7), to bring Hα- and UV-based SFRs into agreement when assuming constant star formation histories. Implementing this assumption into our SFR functions would imply a big shift of ~+0.5 dex at the high end of the SFR function at $z \sim 4$, resulting in similar SFR functions at $z \sim 2$ and $z \sim 4$ (see Figure 12). As a consequence, the total star formation rate density does not decline after $z \sim 2$, but plateaus out to $z \sim 4$ and declines at $z \gtrsim 5$.

The systematic uncertainty in the present SFR function will be alleviated when more observations with new generation submillimeter facilities such as ALMA become available over the next few years.

Table 7
Stepwise Determinations of the SFR Function at $z \sim 4$, $z \sim 5$, $z \sim 6$, $z \sim 7$, and $z \sim 8$: SMC Dust Correction

$\log_{10}$ SFR ($M_\odot$ yr^{-1})	$\phi_{\rm SFR}$ (Mpc^{-3}dex^{-1})
$z \sim 4$	
-0.76 ± 0.02	0.058688 ± 0.018393
-0.33 ± 0.02	0.056971 ± 0.008112
-0.01 ± 0.02	0.024028 ± 0.005114
0.21 ± 0.03	0.015637 ± 0.002376
0.43 ± 0.03	0.012133 ± 0.001011
0.65 ± 0.03	0.006738 ± 0.000576
0.87 ± 0.03	0.005570 ± 0.000416
1.10 ± 0.03	0.003808 ± 0.000254
1.32 ± 0.03	0.001519 ± 0.000141
1.54 ± 0.03	0.000879 ± 0.000089
1.77 ± 0.03	0.000299 ± 0.000051
1.99 ± 0.03	0.000034 ± 0.000020
2.21 ± 0.03	0.000007 ± 0.000009
$z \sim 5$	
-0.61 ± 0.02	0.057283 ± 0.016809
-0.18 ± 0.02	0.019776 ± 0.004047
0.26 ± 0.03	0.010087 ± 0.001221
0.60 ± 0.03	0.004661 ± 0.000382
0.82 ± 0.03	0.002949 ± 0.000209
1.05 ± 0.03	0.002274 ± 0.000148
1.27 ± 0.03	0.001489 ± 0.000101
1.50 ± 0.03	0.000582 ± 0.000055
1.73 ± 0.03	0.000222 ± 0.000031
1.96 ± 0.03	0.000074 ± 0.000018
2.18 ± 0.03	0.000013 ± 0.000007
2.41 ± 0.04	0.000004 ± 0.000004
$z \sim 6$	
-0.47 ± 0.02	0.032668 ± 0.010059
-0.05 ± 0.03	0.015293 ± 0.003159
0.40 ± 0.04	0.004192 ± 0.000706
0.75 ± 0.05	0.002675 ± 0.000294
0.98 ± 0.05	0.001474 ± 0.000175
1.22 ± 0.05	0.000670 ± 0.000086
1.46 ± 0.06	0.000366 ± 0.000052
1.70 ± 0.06	0.000110 ± 0.000025
1.94 ± 0.06	0.000031 ± 0.000012
2.18 ± 0.06	0.000004 ± 0.000004
$z \sim 7$	
-0.42 ± 0.03	0.020132 ± 0.006963
0.01 ± 0.05	0.013461 ± 0.003365
0.34 ± 0.06	0.003842 ± 0.001070
0.57 ± 0.07	0.001984 ± 0.000387
0.80 ± 0.08	0.001410 ± 0.000216
1.03 ± 0.08	0.000659 ± 0.000130
1.27 ± 0.08	0.000408 ± 0.000072
1.51 ± 0.09	0.000101 ± 0.000032
1.75 ± 0.09	0.000069 ± 0.000019
1.98 ± 0.09	0.000002 ± 0.000004
$z \sim 8$	
-0.12 ± 0.12	0.006478 ± 0.002459
0.31 ± 0.15	0.002470 ± 0.000792
0.63 ± 0.16	0.001222 ± 0.000518
0.85 ± 0.17	0.000750 ± 0.000236
1.08 ± 0.18	0.000135 ± 0.000058
1.30 ± 0.18	0.000129 ± 0.000033
1.52 ± 0.19	0.000029 ± 0.000011
1.75 ± 0.19	0.000011 ± 0.000007

Note.
These Schechter parameters are obtained following the procedure described by Smit et al. (2012). We assume an SMC dust correction (Equation (5)) and adopt the linear relation between the UV-continuum slope β and UV luminosity found by Bouwens et al. (2014) (see Section 6.2) and we assume the Kennicutt (1998) conversion from UV to SFR (Equation (1)).

Table 8
Schechter Parameters of the SFR Functions: M99 Dust Correction

$\langle z \rangle$	$\log_{10} \frac{\rm SFR^*}{M_\odot\ {\rm yr}^{-1}}$	$\phi^*_{\rm SFR}$ (10^{-3} Mpc^{-3})	$\alpha_{\rm SFR}$
3.8	1.74 ± 0.07	$1.62^{+0.28}_{-0.24}$	-1.53 ± 0.05
4.9	1.87 ± 0.08	$0.59^{+0.14}_{-0.11}$	-1.60 ± 0.07
5.9	1.75 ± 0.14	$0.36^{+0.16}_{-0.12}$	-1.63 ± 0.14
6.8	1.68 ± 0.20	$0.23^{+0.16}_{-0.09}$	-1.73 ± 0.21
7.9	1.43 ± 0.38	$0.16^{+0.18}_{-0.09}$	-1.85 ± 0.38

Note.
These Schechter parameters are obtained following the procedure described by Smit et al. (2012). We assume a Meurer et al. (1999) dust correction and adopt the linear relation between the UV-continuum slope β and UV luminosity found by Bouwens et al. (2014) (see Section 6.2.). Moreover, we assume a 0.07 dex increase on the Kennicutt (1998) conversion from UV to SFR to better match the instantaneous Hα star formation rates (see Section 6.2).

7. SUMMARY

In this paper we make use of a large sample of galaxies with spectroscopic redshifts between $z = 3.8$–5.0, where Hα can be inferred from the excess in the 3.6 μm *Spitzer*/IRAC band, and also use a photometric sample in the same redshift range. As in previous studies (e.g., Shim et al. 2011; Stark et al. 2013) we find a typical rest-frame Hα EW of ~400 Å for a spectroscopic $z = 3.8$–5.0 sample. In addition, we conduct a systematic investigation of the Hα EWs in the pure photometric-redshift-selected $z \sim 3.8$–5.0 sample and find similar results for both samples (see also Rasappu et al. 2015; Mármol-Queraltó et al. 2016). While we find no strong dependence of the Hα EWs on UV luminosity, UV slope, half-light radius, or Sérsic index, we do find a clear relation between EW$_0$(Hα+[N II] +[S II]) and mass-to-light ratio, $M_*/L_{\rm UV}$ (Figure 3).

We explore the use of the inferred Hα fluxes to derive star formation rates for galaxies in our samples. We compare these Hα-based SFRs with UV-based SFRs using the Meurer et al. (1999) relation and find a strong correlation between the two estimates. However, even when we assume similar extinction toward nebular regions and stellar populations, i.e., $A_{V,\rm stars} = A_{V,\rm gas}$, we still find a small systematic offset ~0.10–0.16 dex in the SFR$_{\rm H\alpha}$/SFR$_{\rm UV+\beta}$ ratios of both our samples.

In this paper, we consider the impact of the assumed dust law, SFH, and the shape of the ionizing spectrum on the SFR$_{\rm H\alpha}$/SFR$_{\rm UV+\beta}$ ratio. Here we provide a summary of our conclusions:

1. *Dust law:* The largest uncertainty in our UV-based SFRs is the dust law. While one issue is the reddening law, another issue is a potential evolution in the intrinsic color of galaxies (prior to the impact of dust reddening). In particular, galaxies with low metallicities and young ages can have bluer intrinsic UV slopes than those of the galaxies in the Meurer et al. (1999) calibration, which could result in an underestimate of the dust content in our galaxies. We investigate the typical intrinsic UV-continuum slope needed to explain the offsets in Hα- and UV-based SFRs and find $A_{1600} = 1.99(\beta + 2.5)$. This dust correction is in agreement with FIR stacking measurements (Coppin et al. 2015), but differs quite strongly from recent ALMA measurements (e.g., Capak

Table 9
Stepwise Determinations of the SFR Function at $z \sim 4$, $z \sim 5$, $z \sim 6$, $z \sim 7$, and $z \sim 8$: M99 Dust Correction

$\log_{10}$ SFR ($M_\odot$ yr^{-1})	$\phi_{\rm SFR}$ (Mpc^{-3}dex^{-1})
$z \sim 4$	
−0.63 ± 0.04	0.055128 ± 0.017277
−0.17 ± 0.04	0.053183 ± 0.007573
0.18 ± 0.05	0.022292 ± 0.004744
0.42 ± 0.05	0.014455 ± 0.002196
0.66 ± 0.05	0.011193 ± 0.000933
0.90 ± 0.05	0.006207 ± 0.000530
1.14 ± 0.05	0.005127 ± 0.000383
1.38 ± 0.05	0.003503 ± 0.000233
1.62 ± 0.05	0.001397 ± 0.000130
1.86 ± 0.05	0.000809 ± 0.000082
2.11 ± 0.06	0.000275 ± 0.000047
2.35 ± 0.06	0.000031 ± 0.000018
2.59 ± 0.06	0.000006 ± 0.000008
$z \sim 5$	
−0.49 ± 0.04	0.053846 ± 0.015801
−0.03 ± 0.05	0.018326 ± 0.003750
0.45 ± 0.05	0.009254 ± 0.001120
0.82 ± 0.06	0.004252 ± 0.000349
1.06 ± 0.06	0.002683 ± 0.000190
1.31 ± 0.06	0.002066 ± 0.000135
1.56 ± 0.06	0.001352 ± 0.000092
1.81 ± 0.06	0.000529 ± 0.000050
2.06 ± 0.06	0.000201 ± 0.000028
2.31 ± 0.06	0.000068 ± 0.000016
2.56 ± 0.06	0.000012 ± 0.000006
2.82 ± 0.06	0.000004 ± 0.000004
$z \sim 6$	
−0.39 ± 0.03	0.031227 ± 0.009615
0.07 ± 0.06	0.014083 ± 0.002909
0.56 ± 0.08	0.003761 ± 0.000633
0.95 ± 0.09	0.002365 ± 0.000260
1.22 ± 0.10	0.001296 ± 0.000154
1.49 ± 0.10	0.000588 ± 0.000075
1.77 ± 0.10	0.000321 ± 0.000046
2.04 ± 0.10	0.000096 ± 0.000022
2.32 ± 0.10	0.000027 ± 0.000011
2.59 ± 0.10	0.000004 ± 0.000004
$z \sim 7$	
−0.32 ± 0.06	0.019064 ± 0.006594
0.13 ± 0.10	0.012464 ± 0.003116
0.50 ± 0.13	0.003480 ± 0.000969
0.75 ± 0.14	0.001773 ± 0.000346
1.01 ± 0.15	0.001252 ± 0.000191
1.27 ± 0.15	0.000582 ± 0.000115
1.54 ± 0.16	0.000360 ± 0.000063
1.81 ± 0.16	0.000089 ± 0.000028
2.08 ± 0.16	0.000061 ± 0.000017
2.35 ± 0.16	0.000002 ± 0.000004
$z \sim 8$	
−0.01 ± 0.24	0.006130 ± 0.002327
0.44 ± 0.28	0.002311 ± 0.000741
0.79 ± 0.31	0.001131 ± 0.000479
1.03 ± 0.32	0.000689 ± 0.000216
1.27 ± 0.33	0.000123 ± 0.000053
1.52 ± 0.34	0.000118 ± 0.000031
1.77 ± 0.34	0.000026 ± 0.000010
2.01 ± 0.34	0.000010 ± 0.000006

Note.
These SFR functions are obtained following the procedure described by Smit et al. (2012). We dust-correct the stepwise UV LFs by Bouwens et al. (2015) using the Meurer et al. (1999) IRX-β relationship. We adopt the linear relation between the UV-continuum slope β and UV luminosity found by Bouwens et al. (2014) (see Section 6.2.). Moreover, we assume a 0.07 dex increase on the Kennicutt (1998) conversion from UV to SFR to better match the instantaneous Hα star formation rates (see Section 6.2).

et al. 2015; Aravena et al. 2016; Bouwens et al. 2016a; Dunlop et al. 2016). Assuming an SMC dust law such as that favored by Capak et al. (2015) and Bouwens et al. (2016a) the $\rm SFR_{H\alpha}/SFR_{UV+\beta}$ ratio could be offset by ∼0.2 dex (assuming $A_{V,\rm stars} = A_{V,\rm gas}$).

2. *Bursty SFH:* A natural consequence of bursty star formation histories is the production of high-Hα EWs and high $\rm SFR_{H\alpha}/SFR_{UV+\beta}$ ratios for short (∼5 Myr) time periods. However, we find comparable $\rm SFR_{H\alpha}/SFR_{UV+\beta}$ for both our spectroscopic-redshift and the photometric-redshift sample, and even a mass-limited photometric subsample. We use a Monte Carlo simulation to compare the expected sSFRs from Hα and UV indicators with our samples. We find that a sample of galaxies with typical burst masses of $M_{\rm burst} \sim 10^8\,M_\odot$ and burst intervals of $\rm dt_{burst} \sim 5$–10Myr can produce a ∼0.1 dex offset in $\rm SFR_{H\alpha}/SFR_{UV+\beta}$. However, we also find a low $\rm sSFR_{H\alpha}$ tail in our simulated distribution that is ∼2× larger than what we find in our observed sample, which argues against significantly bursty star formation histories.
3. *Rising SFH:* Rising star formation histories create an offset in the $\rm SFR_{H\alpha}/SFR_{UV+\beta}$ ratio owing to the different timescales of star formation probed by Hα (∼10 Myr) and UV (∼100 Myr) SFR indicators. We estimate that this offsets the $\rm SFR_{H\alpha}/SFR_{UV+\beta}$ ratio by ∼0.1 dex, using prescriptions given in Reddy et al. (2012).
4. *Production Efficiency for Ionizing Photons/Ionizing Spectrum:* The shape of the ionizing radiation field for low-metallicity stellar populations is currently poorly constrained, which is unfortunate since this can have a significant impact on the nebular emission of high-redshift galaxies (e.g., Kewley et al. 2013). We investigate two sets of models that include the effects of stellar rotation (Leitherer et al. 2014) and the effects of massive binary star systems (Eldridge & Stanway 2012) on low metallicity. We find that these models can generate an observed offset in the $\rm SFR_{H\alpha}/SFR_{UV+\beta}$ ratio of ∼0.1–0.3 dex. We argue that if high-redshift UV-selected galaxies prefer an SMC type dust law, some additional source of ionizing photons is required, e.g., a rising SFH, to explain the strength of the Hα emission lines we observe.

We find that there are two flavors of physical models that appear plausible on the basis of the observations we consider (Table 4), the first invoking a Meurer et al. (1999) dust calibration with a $A_{V,\rm stars} = A_{V,\rm gas}$ and correcting up UV-based, time-averaged SFR estimates by ∼0.1 dex to better match the instantaneous SFRs and the second invoking a SMC dust law with $A_{V,\rm stars} = A_{V,\rm gas}$ and supposing that $z \sim 4$ galaxies are more efficient at producing ionizing photons than galaxies in standard stellar population models (see Bouwens et al. 2016b; Stark et al. 2015, 2016, for a discussion of the impact this may have on galaxies' capability to reionize the universe).

We adopt the latter flavor of physical model as our fiducial one (and include some results from the former model in Appendix B). We use this model to construct the main sequence of star-forming galaxies from our Hα-based SFRs (Section 6.1). When we take into account the incompleteness at the faint end of our selection, we find that the slope is broadly consistent with the unity low-mass slope found by Whitaker et al. (2014) at $z \sim 0.5$–2.5. Furthermore, we find an intrinsic scatter of $\sigma \sim 0.4$ and a normalization of the main sequence of $\log_{10}$ sSFR$_{\rm H\alpha}$/Gyr$^{-1} = 0.47 \pm 0.06$, in reasonable agreement with recent determinations from SED fitting (e.g., Duncan et al. 2014; González et al. 2014; Salmon et al. 2015).

In Section 6.2, we follow the Smit et al. (2012) procedure to infer SFR functions at $z \sim 4$–8 from the UV luminosity functions derived by Bouwens et al. (2015), and the UV-continuum slopes derived by Bouwens et al. (2014). Consistent with our fiducial approach, we use a SMC-type dust calibration and we assume the Kennicutt (1998) conversion factor between UV and SFR, given that the effects of an increased production efficiency of ionizing photons and a rising SFH roughly cancel each other out (see also Mashian et al. 2016). The $z = 4$–8 SFR functions for a Meurer et al. (1999) dust correction are presented in Appendix B.

We conclude that systematic use of Hα SFRs inferred from *Spitzer*/IRAC photometry provides an exciting opportunity to unravel fundamental properties of the high-redshift galaxy population in advance of *JWST*.

We thank Selma de Mink, Carlos Frenk, Ylva Götberg, John Lucey, and Tom Theuns for interesting conversations. This work was supported by the Leverhulme Trust.

APPENDIX A
TESTING OUR METHOD TO EXTRACT LINE FLUXES FROM PHOTOMETRIC OBSERVATIONS

To validate our method of inferring Hα using the *Spitzer*/IRAC photometry, we perform two tests at $z < 3.8$. First, we assemble a small sample of lower redshift galaxies with emission line measurements obtained directly from spectroscopy and compare these measurements with the values inferred from the flux offset in the contaminated band from the continuum SED. We use a sample of line emitters selected from the 3D-*HST* grism survey presented by Momcheva et al. (2016) at $z = 1.3$–1.5 where Hα, [N II], and [S II] contaminate the H_{160} band. From the 3D-*HST* survey we select sources with a $>5\sigma$ detection of the Hα+[N II] blended emission lines, a $>5\sigma$ detection in the K band (the adjacent band to the H_{160} band used to derive emission lines) and a V_{606}-band total magnitude brighter than 26.5 mag (the V_{606} band at $z = 1.3$–1.5 corresponds to roughly the same rest-frame wavelength as the H_{160} band at $z = 3.8$–5.0).

For this sample of 160 sources we use the same photometry as described in Section 2.1 and we perform the same steps in deriving the SED inferred line fluxes as described in Section 3. We do not include photometry bands contaminated with strong emission lines and we assume the same fixed line ratios between Hα, [N II], and [S II] as in our main sample and correct the Hα+[N II] measurement by 10% to account for the flux of [S II] (the grism measurements of this line are highly uncertain or not detected at all). We present the results of our inferred line fluxes in the left panel of Figure 13. We find a median difference of -0.01 ± 0.02 dex (uncertainty obtained through bootstrapping) between the line fluxes measured with spectroscopy and those inferred from the photometry.

For our second test we collected a sample of spectroscopically confirmed galaxies between $z = 3.0$–3.8, using the same public redshift catalogs of Balestra et al. (2010)

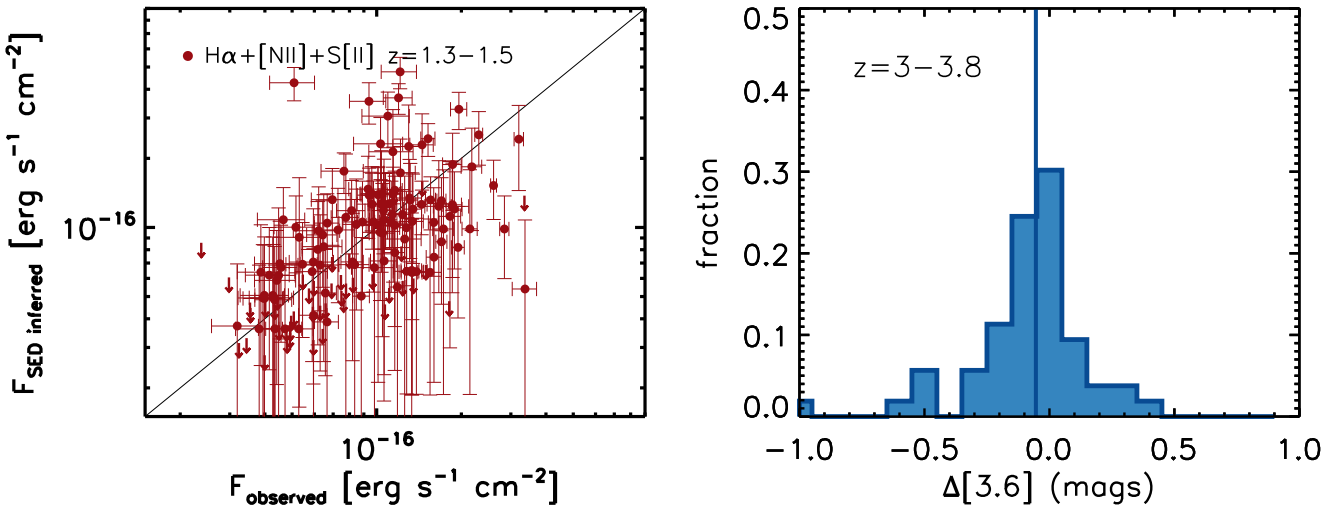

Figure 13. Left panel: a test of our inferred emission line method using galaxies at $z = 1.3$–1.5 (Momcheva et al. 2016) where the the Hα+[N II]+[S II] lines contaminate the H_{160} band. The line fluxes inferred from the photometry are −0.01 dex offset in the median source from the spectroscopic measurements. Right panel: the 3.6 μm excess flux measurements of a spectroscopic sample at $z = 3.0$–3.8, where the 3.6 μm band is unaffected by strong emission lines and should therefore show no offsets from the predicted continuum flux. The sample is −0.05 magnitude or −0.02 dex below the predicted continuum flux in the median source.

and Vanzella et al. (2005, 2006, 2008) over the GOODS-S field that were used for our spectroscopic sample described in Section 2.1. For this sample we test the the same methods and photometry that we used in our paper for our spectroscopic $z = 3.8$–5.0 galaxy sample by deriving the offset in the 3.6 μm band flux from the predicted continuum flux; given the lack of line contamination at $z = 3.0$–3.8, this value should be approximately zero. An important difference for the $z = 3.0$–3.8 samples is that 70% and 90% of the galaxies have contaminated photometry from the [O III] and [O II] emission lines, respectively, while for the $z = 3.8$–5.0 sample only 43% of all the galaxies can have affected photometry, due to the flux of the [O II] emission lines. Since the photometry of the $z = 3.0$–3.8 sample is significantly affected by emission lines, we exclude the JH_{140}, H_{160}, and K_s bands from the SED fitting, but otherwise keep all steps identical to the procedures described in Sections 2.1–3.

The results of the offsets between the 3.6 μm-band flux and the predicted continuum flux is presented in the right panel of Figure 13. We find a small median offset of -0.05 ± 0.01 magnitude or -0.02 ± 0.01 dex (uncertainty obtained through bootstrapping) in our $z = 3.0$–3.8 spectroscopic galaxy sample, with a modest standard deviation of 0.23 magnitude or 0.09 dex.

Both these test results indicate that there are no obvious systematics present in our photometry that would cause us to *overestimate* the inferred Hα flux, given our method. We remark, however, that it is possible that we might be underestimating the derived Hα luminosity. This underestimate, if real, would strengthen our conclusion that there are small systematic differences between Hα- and UV-based SFRs given standard low-redshift calibrations.

APPENDIX B
SFR FUNCTIONS ASSUMING SMC DUST CORRECTION

In this appendix we present SFR functions as described in Section 6.2 and using the Meurer et al. (1999) dust correction in Equation (2). These results correspond to the second fiducial model presented in Table 4.

In deriving the SFR functions, we dust-correct the UV continuum light using an SMC extinction law and do not make any further corrections. In addition, we convert the UV luminosities into SFR using Equation (1) (Equation (3) overpredicts the Hα SFR by ~0.2 dex). In doing so, we rely on the conclusions from Sections 5.1–5.3 where we found that a combination of rising star formation histories and low-metallicity stellar population models including stellar rotation can bring Hα- and UV-based SFR estimates into good agreement.

REFERENCES

Álvarez-Márquez, J., Burgarella, D., Heinis, S., et al. 2016, A&A, 587, A122
Anders, P., & Fritze-v. Alvensleben, U. 2003, A&A, 401, 1063
Aravena, M., Decarli, R., Walter, F., et al. 2016, arXiv:1607.06769
Ashby, M. L. N., Willner, S. P., Fazio, G. G., et al. 2013, ApJ, 769, 80
Ashby, M. L. N., Willner, S. P., Fazio, G. G., et al. 2015, ApJS, 218, 33
Balestra, I., Mainieri, V., Popesso, P., et al. 2010, A&A, 512, A12
Bertin, E., & Arnouts, S. 1996, A&AS, 117, 393
Bourne, N., Dunlop, J. S., Merlin, E., et al. 2016, arXiv:1607.04283
Bouwens, R., Aravena, M., Decarli, R., et al. 2016a, submitted (arXiv:1606.05280)
Bouwens, R. J., Illingworth, G. D., Franx, M., et al. 2009, ApJ, 705, 936
Bouwens, R. J., Illingworth, G. D., Oesch, P. A., et al. 2012, ApJ, 754, 83
Bouwens, R. J., Illingworth, G. D., Oesch, P. A., et al. 2014, ApJ, 793, 115
Bouwens, R. J., Illingworth, G. D., Oesch, P. A., et al. 2015, ApJ, 803, 34
Bouwens, R. J., Smit, R., Labbe, I., et al. 2016b, ApJ, 831, 176
Brammer, G. B., van Dokkum, P. G., & Coppi, P. 2008, ApJ, 686, 1503
Calzetti, D. 1997, AJ, 113, 162
Calzetti, D., Armus, L., Bohlin, R. C., et al. 2000, ApJ, 533, 682
Capak, P. L., Carilli, C., Jones, G., et al. 2015, Natur, 522, 455
Castellano, M., Fontana, A., Grazian, A., et al. 2012, A&A, 540, A39
Castellano, M., Sommariva, V., Fontana, A., et al. 2014, A&A, 566, A19
Cooray, A., Calanog, J., Wardlow, J. L., et al. 2014, ApJ, 790, 40
Coppin, K. E. K., Geach, J. E., Almaini, O., et al. 2015, MNRAS, 446, 1293
Dayal, P., Dunlop, J. S., Maio, U., & Ciardi, B. 2013, MNRAS, 434, 1486
Dayal, P., & Ferrara, A. 2012, MNRAS, 421, 2568
de Barros, S., Schaerer, D., & Stark, D. P. 2014, A&A, 563, A81
de Mink, S. E., Cantiello, M., Langer, N., et al. 2009, A&A, 497, 243
Domínguez, A., Siana, B., Brooks, A. M., et al. 2015, MNRAS, 451, 839
Duncan, K., Conselice, C. J., Mortlock, A., et al. 2014, MNRAS, 444, 2960
Dunlop, J. S., McLure, R. J., Biggs, A. D., et al. 2016, arXiv:1606.00227
Dunlop, J. S., McLure, R. J., Robertson, B. E., et al. 2012, MNRAS, 420, 901
Dunlop, J. S., Rogers, A. B., McLure, R. J., et al. 2013, MNRAS, 432, 3520
Eldridge, J. J., & Stanway, E. R. 2012, MNRAS, 419, 479
Erb, D. K., Steidel, C. C., Shapley, A. E., et al. 2006, ApJ, 647, 128
Eyles, L. P., Bunker, A. J., Stanway, E. R., et al. 2005, MNRAS, 364, 443
Finkelstein, S. L., Papovich, C., Dickinson, M., et al. 2013, Natur, 502, 524
Finkelstein, S. L., Papovich, C., Salmon, B., et al. 2012, ApJ, 756, 164
Fontana, A., Dunlop, J. S., Paris, D., et al. 2014, A&A, 570, A11
Fumagalli, M., Patel, S. G., Franx, M., et al. 2012, ApJL, 757, L22
González, V., Bouwens, R., Illingworth, G., et al. 2014, ApJ, 781, 34
González, V., Bouwens, R. J., Labbé, I., et al. 2012, ApJ, 755, 148
González, V., Labbé, I., Bouwens, R. J., et al. 2010, ApJ, 713, 115
Hathi, N. P., Mobasher, B., Capak, P., Wang, W.-H., & Ferguson, H. C. 2012, ApJ, 757, 43
Kajisawa, M., Konishi, M., Suzuki, R., et al. 2006, PASJ, 58, 951
Kelly, B. C. 2007, ApJ, 665, 1489
Kennicutt, R. C., Jr. 1998, ARA&A, 36, 189
Kewley, L. J., Dopita, M. A., Leitherer, C., et al. 2013, ApJ, 774, 100
Knudsen, K. K., Richard, J., Kneib, J.-P., et al. 2016, MNRAS, 462, L6
Kriek, M., van Dokkum, P. G., Labbé, I., et al. 2009, ApJ, 700, 221
Labbé, I., Bouwens, R., Illingworth, G. D., & Franx, M. 2006, ApJL, 649, L67
Labbé, I., González, V., Bouwens, R. J., et al. 2010a, ApJL, 716, L103
Labbé, I., González, V., Bouwens, R. J., et al. 2010b, ApJL, 708, L26
Labbé, I., Oesch, P. A., Bouwens, R. J., et al. 2013, ApJL, 777, L19
Labbé, I., Oesch, P. A., Illingworth, G. D., et al. 2015, ApJS, 221, 23
Leitherer, C., Ekström, S., Meynet, G., et al. 2014, ApJS, 212, 14
Leitherer, C., & Heckman, T. M. 1995, ApJS, 96, 9
Leitherer, C., Schaerer, D., Goldader, J. D., et al. 1999, ApJS, 123, 3
Magnelli, B., Elbaz, D., Chary, R. R., et al. 2011, A&A, 528, A35
Maiolino, R., Nagao, T., Grazian, A., et al. 2008, A&A, 488, 463
Mannucci, F., Cresci, G., Maiolino, R., et al. 2009, MNRAS, 398, 1915
Mármol-Queraltó, E., McLure, R. J., Cullen, F., et al. 2016, MNRAS, 460, 3587
Mashian, N., Oesch, P. A., & Loeb, A. 2016, MNRAS, 455, 2101
Meurer, G. R., Heckman, T. M., & Calzetti, D. 1999, ApJ, 521, 64
Momcheva, I. G., Brammer, G. B., van Dokkum, P. G., et al. 2016, ApJS, 225, 27
Oesch, P. A., Labbé, I., Bouwens, R. J., et al. 2013, ApJ, 772, 136
Oesch, P. A., van Dokkum, P. G., Illingworth, G. D., et al. 2015, ApJL, 804, L30
Oke, J. B., & Gunn, J. E. 1983, ApJ, 266, 713
Oteo, I. 2014, A&A, 572, L4
Pannella, M., Elbaz, D., Daddi, E., et al. 2015, ApJ, 807, 141
Prevot, M. L., Lequeux, J., Prevot, L., Maurice, E., & Rocca-Volmerange, B. 1984, A&A, 132, 389
Ramírez-Agudelo, O. H., Simón-Díaz, S., Sana, H., et al. 2013, A&A, 560, A29
Rasappu, N., Smit, R., Labbe, I., et al. 2015, MNRAS, 461, 3886
Reddy, N., Dickinson, M., Elbaz, D., et al. 2012, ApJ, 744, 154
Reddy, N. A., Erb, D. K., Pettini, M., Steidel, C. C., & Shapley, A. E. 2010, ApJ, 712, 1070
Reddy, N. A., Steidel, C. C., Pettini, M., et al. 2008, ApJS, 175, 48
Retzlaff, J., Rosati, P., Dickinson, M., et al. 2010, A&A, 511, A50
Roberts-Borsani, G. W., Bouwens, R. J., Oesch, P. A., et al. 2016, ApJ, 823, 143
Salmon, B., Papovich, C., Finkelstein, S. L., et al. 2015, ApJ, 799, 183
Salpeter, E. E. 1955, ApJ, 121, 161
Sana, H., de Mink, S. E., de Koter, A., et al. 2012, Sci, 337, 444
Sanders, R. L., Shapley, A. E., Kriek, M., et al. 2015, ApJ, 799, 138
Schaerer, D., Boone, F., Zamojski, M., et al. 2015, A&A, 574, A19

Schaerer, D., & de Barros, S. 2009, A&A, 502, 423
Schenker, M. A., Ellis, R. S., Konidaris, N. P., & Stark, D. P. 2013, ApJ, 777, 67
Shim, H., Chary, R.-R., Dickinson, M., et al. 2011, ApJ, 738, 69
Shirazi, M., Brinchmann, J., & Rahmati, A. 2014, ApJ, 787, 120
Shivaei, I., Reddy, N. A., Steidel, C. C., & Shapley, A. E. 2015, ApJ, 804, 149
Skelton, R. E., Whitaker, K. E., Momcheva, I. G., et al. 2014, ApJS, 214, 24
Smit, R., Bouwens, R. J., Franx, M., et al. 2012, ApJ, 756, 14
Smit, R., Bouwens, R. J., Franx, M., et al. 2015, ApJ, 801, 122
Smit, R., Bouwens, R. J., Labbé, I., et al. 2014, ApJ, 784, 58
Sobral, D., Best, P. N., Smail, I., et al. 2014, MNRAS, 437, 3516
Sparre, M., Hayward, C. C., Feldmann, R., et al. 2015, MNRAS, in press (arXiv: 1510.03869)
Speagle, J. S., Steinhardt, C. L., Capak, P. L., & Silverman, J. D. 2014, ApJS, 214, 15
Spitler, L. R., Labbé, I., Glazebrook, K., et al. 2012, ApJL, 748, L21
Stark, D. P., Ellis, R. S., Bunker, A., et al. 2009, ApJ, 697, 1493
Stark, D. P., Ellis, R. S., Charlot, S., et al. 2016, arXiv:1606.01304
Stark, D. P., Schenker, M. A., Ellis, R., et al. 2013, ApJ, 763, 129
Stark, D. P., Walth, G., Charlot, S., et al. 2015, MNRAS, 454, 1393
Steidel, C. C., Rudie, G. C., Strom, A. L., et al. 2014, ApJ, 795, 165
Troncoso, P., Maiolino, R., Sommariva, V., et al. 2014, A&A, 563, A58
van der Wel, A., Bell, E. F., Häussler, B., et al. 2012, ApJS, 203, 24
van der Wel, A., Franx, M., van Dokkum, P. G., et al. 2014, ApJ, 788, 28
Vanzella, E., Cristiani, S., Dickinson, M., et al. 2005, A&A, 434, 53
Vanzella, E., Cristiani, S., Dickinson, M., et al. 2006, A&A, 454, 423
Vanzella, E., Cristiani, S., Dickinson, M., et al. 2008, A&A, 478, 83
Vanzella, E., Giavalisco, M., Dickinson, M., et al. 2009, ApJ, 695, 1163
Verma, A., Lehnert, M. D., Förster Schreiber, N. M., Bremer, M. N., & Douglas, L. 2007, MNRAS, 377, 1024
Watson, D., Christensen, L., Knudsen, K. K., et al. 2015, Natur, 519, 327
Whitaker, K. E., Franx, M., Leja, J., et al. 2014, ApJ, 795, 104
Wiklind, T., Dickinson, M., Ferguson, H. C., et al. 2008, ApJ, 676, 781
Wilkins, S. M., Bunker, A., Coulton, W., et al. 2013a, MNRAS, 430, 2885
Wilkins, S. M., Bunker, A. J., Stanway, E., Lorenzoni, S., & Caruana, J. 2011, MNRAS, 417, 717
Wilkins, S. M., Coulton, W., Caruana, J., et al. 2013b, MNRAS, 435, 2885
Wilkins, S. M., Gonzalez-Perez, V., Lacey, C. G., & Baugh, C. M. 2012, MNRAS, 424, 1522
Yabe, K., Ohta, K., Iwata, I., et al. 2009, ApJ, 693, 507
Zeimann, G. R., Ciardullo, R., Gebhardt, H., et al. 2014, ApJ, 790, 113
Zitrin, A., Labbé, I., Belli, S., et al. 2015, ApJL, 810, L12